ELSEVIER

Check for updates

RESEARCH: Review

# Advances in three-component plasmonic-assisted heterostructures for enhanced photocatalysis and photoelectrochemical catalysis

**Chengyu Ji, Haochen Zhou, Sixing Tang, Pankaj Sharma, Mary P. Ryan, D. Jason Riley, Fang Xie** *

Department of Materials and London Centre for Nanotechnology, Imperial College London, London SW7 2AZ, UK

**Traditional semiconductor materials such as metal-oxide-based photoelectrodes have been extensively explored for energy and environmental applications. However, their performance is hindered by poor light absorption, high charge recombination rates, and low surface kinetics. The incorporation of metal–organic framework (MOF) and plasmonic structures into semiconductors is one of the most promising strategies to achieve performances beyond those of bare MOF and/or conventional semiconductors. This review summarises the rational design of semiconductor-based photoelectrodes incorporating MOFs and plasmonic metals for hybrid photoelectrochemical catalysis and photocatalysis, with a wide variety of parameters including photoactivity, conductivity, catalytic property, surface morphology, porous architecture and bandgap alignment. Moreover, applications of this new generation of composite photoelectrodes in water splitting, $CO_2$ reduction and pollution degradation are discussed in detail. The challenges and prospects of plasmonic MOF nanocomposites in eco-friendly and cost-efficient technologies for practical applications in water splitting, $CO_2$ reduction and environmental remediation are also highlighted.**

**Keywords: Plasmonics; Metal–organic framework; Photoelectrochemical water splitting; $CO_2$ reduction; Pollution degradation**

## Introduction

The combustion of fossil fuels has caused global concern about environmental pollution, energy shortages and global warming. It is estimated that fossil fuel usage will increase global temperatures by 1.5 °C in the next 50 years [1], leading to a desire to reduce their usage. Today, fossil fuels are still supporting over 64% of electricity production and 84% of overall energy consumption, creating an urgent need for other environmentally friendly energy sources [2]. Among the various strategies, solar-driven catalysis that converts solar energy into chemicals through water splitting or carbon dioxide ($CO_2$) reduction has attracted tremendous attention [3,4].

Solar-driven catalysis typically adopts either a photocatalytic (PC) or photoelectrolytic (PEC) approach, depending on the position of their energy bands relative to the reaction potentials. This alignment determines the setup of catalytic systems and whether an external bias is necessary [5]. In mechanism, the semiconductor harnesses the energy from incident photons to generate photogenerated charge carriers, which subsequently migrate to the active sites and participate in the reactions [6,7]. The bandgap width directly influences the capacity of semiconductors to absorb photons, and the energy band bending at the semiconductor-electrolyte interface significantly determines the separation and migration of photogenerated charge carriers. Only the minority carriers that generate or diffuse into the space charge region can be effectively separated and transferred within their lifetime [8]. Therefore, most semiconductors cannot meet the industrial scale requirements of 10% solar-to-hydrogen

* Corresponding author.
*E-mail address:* Xie, F. (f.xie@imperial.ac.uk)

1369-7021/© 2023 The Authors. Published by Elsevier Ltd. This is an open access article under the CC BY license (http://creativecommons.org/licenses/by/4.0/).
https://doi.org/10.1016/j.mattod.2023.09.009

(STH) efficiency and 5000 h of durability [3,4]. The narrow spectral light absorption, short charge carrier lifetime and long drift time limit the application of semiconductors, thereby promoting the desire for the development of novel semiconductor-based nanohybrids [9]. Metal-organic frameworks (MOFs) are hybrid organic–inorganic materials formed of organic ligands and metal nodes (clusters) [10]. The encapsulation of MOFs into semiconductors can greatly enhance the activity of photocatalysts by adjusting band structures and enhancing charge/mass transfer. In addition, MOFs provide a variety of powerful pore structures and functional groups on the ligands, to enrich specific adsorption and improve catalytic performance [11]. A tandem configuration of semiconductors/MOFs is commonly utilized, wherein photogenerated electrons and holes migrate to distinct regions to catalyse oxidation and reduction reactions, respectively. If a z-scheme charge transfer can be achieved, the efficiency of charge carrier separation will be substantially enhanced. More importantly, some light-responsive MOFs could improve light harvesting in hybrid photoelectrodes of MOF-semiconductor through "device-by-design" strategies. Hybrid photoelectrodes which couple plasmonic nanostructures with semiconductors is another exciting strategy for dramatically improving photoelectrode performance, in which the plasmonic energy is transferred from the metal nanostructures to the semiconductors. The plasmon-induced properties decay rapidly away from the plasmonic surface, and the responses with nonadsorbing molecules are generally very weak [12]. MOF-semiconductor heterojunctions could potentially absorb broadband light. However, the two-step photon absorption undermines the efficiency and results in inadequate photoelectrochemical (PEC) performance. A plasmonic nanostructure-MOF-semiconductor tri-phase hybrid platform can address these issues. In the hierarchical plasmonic nanostructure-MOF-semiconductor platform, energy band alignment can be finely tailored. The electronic structure could be optimized by the incorporation of plasmonic nanostructures, which boosts photogenerated charge carrier transfer to Fermi levels [13]. The light-responsive MOF could act as both photosensitizer and co-catalyst. The interaction of the three components is expected to form a complete and well-functionalised photoelectrode. The ternary hybrid structures have great potential in photocatalytic or PEC water splitting, $CO_2$ reduction and degradation of pollutants.

This review first demonstrates the fundamentals and mechanisms of selecting MOF and plasmonic nanostructures for composites for photocatalysis and PEC catalysis in Chapter 2. Then, the construction of MOF-semiconductors and plasmonic-enhanced MOF or semiconductor-plasmonics composites are listed and the mechanisms and limitations are discussed. Ternary plasmonic nanostructure-MOF-semiconductor composites are therefore proposed. Design considerations of both binary and ternary systems are summarised and supplement each other in Chapter 3. Existing tri-phase works are reviewed and their potential in various applications including water splitting, $CO_2$ reduction and environmental remediation are evaluated in Chapter 4. The design from unary to binary and ternary compsite photocatalysis and PEC systems is illustrated in Fig. 1.

## Plasmon and MOFs in solar energy conversion: Mechanisms and limitations

MOFs are hybrid organic–inorganic materials coordinated by organic ligands and metal nodes [10]. Most MOFs present high porosity and a large specific surface area. Owing to the flexible choices of metal ion-organic linker coordinations, the crystal, structural and compositional properties of MOFs could be easily tuned. Therefore, MOFs have extensively been reported for use in many applications, including gas separation/absorption [14–16], sensing [17,18], biomedicine [19,20] and catalysis [21].

In addition, many semiconductors have been investigated for photoelectrode applications, such as metal oxides, III-V compounds, metal chalcogenides, metal nitrides and carbon nitrides [22]. Here, MOFs are not classified as semiconductors because the majority of the MOFs behave as electrical insulators with conductivity lower than $10^{-10}$ $Scm^{-1}$ [23].

### *MOFs for photocatalysis/PEC catalysis and mechanisms*

Traditional metal oxide materials such as $TiO_2$ have been extensively explored for photocatalysis and photoelectrochemical catalysis. However, their wide band gaps and slow surface redox reactions have hindered their further commercial applications. Light-responsive MOFs with abundant surface-active sites have huge potential to mitigate these limitations of traditional oxide semiconductors.

In 1999, Yaghi's group successfully synthesized the famous MOF-5. The photocatalysis performance of MOF-5 in phenol degradation was reported for the first time in 2007 [24,25]. Since then, more work has been reported for MOF based photocatalysis and PEC. Generally, MOFs could act as light harvesters to generate electron-hole pairs; or act as co-catalysts, where MOFs do not absorb light but promote photogenerated charge separation or catalytic reactions; or act as a host. Visible-light responsive MOFs with plenty of active sites exposed are ideal candidates for boosting surface redox reactions in constructing hybrid MOF-semiconductor systems.

#### *Light absorption by MOFs*

Generally, light absorption in photoactive MOFs is due to the organic linkers. Most of these photoactive organic ligands are aromatic compounds, which can absorb ultraviolet (UV) or visible light. After the excitation, ligand-localized π-π*-based transitions can occur. Some metal ion/clusters can also absorb photons via ion excitation processes. Take ZIF-67 as an example, it presents an excitation peak at 600 nm from cobalt d-d electronic transitions [26]. After an initial π-π* electronic transition or d-d transition, typical photophysical pathways are metal-to-ligand charge transition (MLCT) and ligand-to-metal charge transition (LMCT).

In the past decade, more than 20,000 types of MOF with different components and structures have been reported [10]. Among all the photo-responsive MOFs, three series of MOFs have been thoroughly investigated for PC or PEC catalysis: UiO-MOFs, ZIF-MOFs, and MIL-MOFs.

UiO-MOFs are built using dicarboxylic acid ligands and $Zr^{4+}$. While original UiO-Xs (X = 66, 67, 68) could only be excited

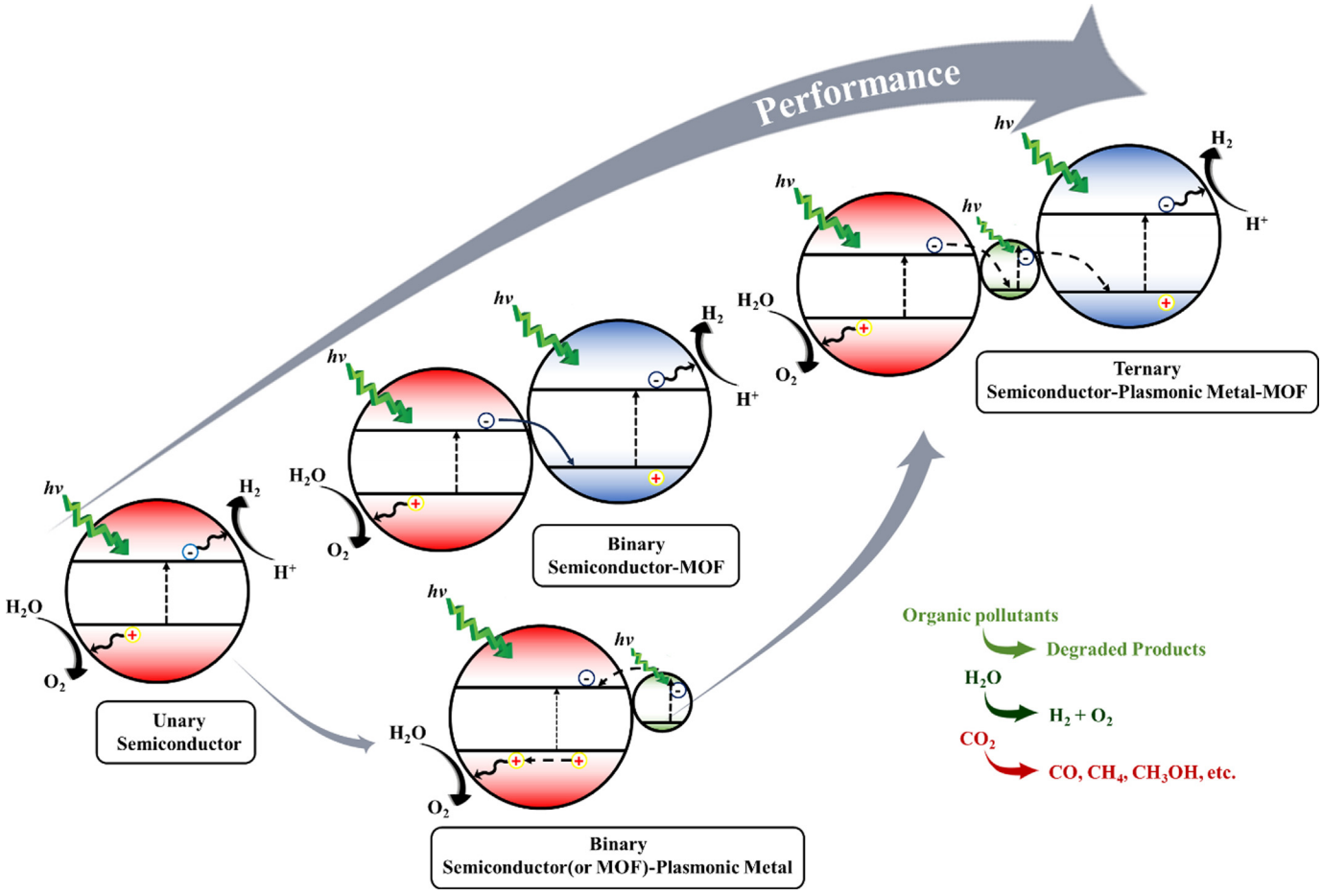


**FIG. 1**

Schematics of unary, binary and ternary photocatalysis and PEC composite structures.

by UV light, the light absorption spectra has been readily expanded to the visible region through ligand group functionalization and metal node composition control, this will be discussed in the next section [27,28].

In zeolitic imidazolate frameworks (ZIFs), transition-metal cations (M) like $Zn^{2+}$ or $Co^{2+}$ ions are connected by imidazole-based ligands (Im). The angle of M-Im-M (~145°) is similar to that of Si-O-Si in silicon-based zeolites [29]. Therefore, ZIFs mirror some features of the zeolite structure, encompassing high porosity, high surface-area-to-volume ratio, and high thermal and chemical stability. Unlike UiO-MOFs, ZIF-67 contains an absorption peak in the visible region of light. It also presents a charge-separated state including a long-lived intermediate state, this together with its porous structure with abundant active sites exposed, makes ZIF-67 a promising candidate for PC/PEC catalysis.

MIL-MOFs could be constructed from different ligands. To illustrate, the MIL-53 family are built from terephthalate and mostly trivalent metal nodes, while the MIL-101 series are crystallized from trimesic acid and metal centres. Owing to their photoactive, minimally toxic and cost-effective features, MIL-MOFs show great potential in photocatalysis. MIL-100(Fe) has been reported for photocatalytic pollutant degradation under visible light and MIL-101(Fe) has been applied for photocatalytic $CO_2$ reduction [30,31].

Typical light responsive MOFs exhibit bandgaps ranging from 1.8 eV (MIL-100) to 3.6 eV (MIL-125), detailed bandgaps and band energies of MOFs are shown in Fig. 2a and discussed in the next section.

It is noteworthy that post-synthetic modification (PSM), can functionalise the MOFs and render them more versatile in composition and properties, specifically changing the bandgap and/or conductivity. For example, the bandgap of UiO-66 drops from 3.05 eV to 2.8 eV after adding an amino group (UiO-66-NH2). Post-synthetic modification (PSM) can be realised by five major methods: (i) physical impregnation, (ii) covalent attachment, (iii) *In situ* reaction, (iv) ligand replacement, and (v) metal addition [32]. A detailed discussion of all these strategies is beyond the scope of this review. We, therefore, refer readers to more specialised reviews on this topic [33,34].

## *Rational design of MOF/semiconductor hybrid photocatalysts/PEC catalysts*

### *Interface – epitaxial matching*

Hybrid materials can be either composites or heterojunction structures. Undoubtedly, heterojunctions with build-in electric fields are potentially superior for charge transfer. However, it is not easy to achieve a perfect lattice match at the interface between a MOF and a semiconductor. The subunits of MOFs are usually much larger than the unit cells of semiconductors.

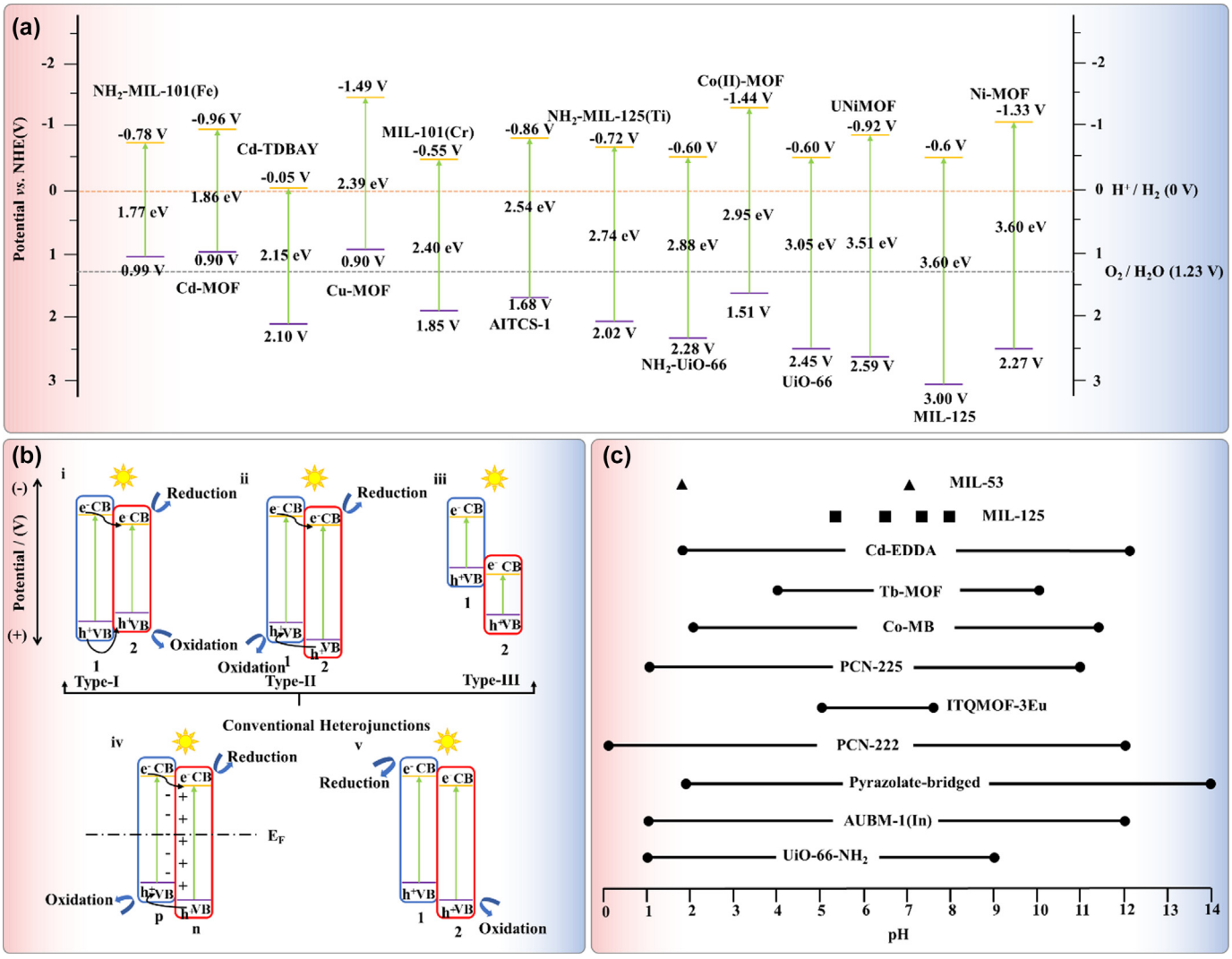


**FIG. 2**

(a) The bandgap and positions of some MOFs [38,39]. (b) Schematic of i. Type-I; ii. Type-II; iii. Type-III; iv. p–n heterojunction; v. Z-scheme heterojunction, where '1' and '2' mean semiconductor 1, semiconductor 2; 'p' and 'n' refer to p-semiconductor and n-semiconductor, respectively [40]. (c) The pH stability of some MOFs [50]. Reproduced with permission from [40,50]. Copyright Royal Society of Chemistry, 2019. Copyright John Wiley & Sons, 2021.

Lattice mismatches higher than 5% do not typically support a semi-coherent or coherent interface. Incoherent interfaces result in poor electronic properties and stability [35]. Even for semi-coherent interfaces, misfit dislocations act as electron-hole recombination centres and junction degradation may occur. Only in a few cases, it is possible to form a 'coherent interface' between one semiconductor and the MOF with the same metal source. To illustrate, a 5*12 expansion of the ZIF-9 (11-1) surface matches well to the 19*20 (1112 CoO with a strain of 0.1%, which is an almost perfect epitaxy [35]. Other $TiO_2$/MIL-125 (Ti) and ZnO/ZIF-8 heterojunctions have also been fabricated for photoelectrochemical catalysis, and excellent water splitting performance and good stability have been obtained [36,37].

*Energy bandgap alignment*

For a single MOF water-splitting photocatalyst, the lowest unoccupied molecular orbital (LUMO) and highest occupied molecular orbital (HOMO) of the MOF should straddle the reduction potential of $H^+/H_2$ (0.0 V *vs*. NHE) and the oxidation potential of $O_2/H_2O$ (1.23 V *vs*. NHE) with or without a bias voltage, implying that the bandgap should be at least larger than 1.23 eV. Fig. 2a shows the conduction and valence band positions of some typical MOFs, such as $NH_2$-MIL-125 and $NH_2$-UiO-66.

Within a MOF/semiconductor hybrid, the band position of the MOF and semiconductor should match well with each other. Some MOFs also behave as semiconductors, with the MOF/semiconductor hybrids containing one of three types of heterojunctions: straddling gap heterojunction (type-I), staggered gap (type-II) heterojunction, broken gap heterojunction (type-III); and two special heterojunctions: p-n heterojunction and direct Z-scheme heterojunction (shown in Fig. 2b) [40,41].

Among the various types of heterostructure, type II, p–n heterojunctions and Z-scheme heterostructures are favourable for PC or PEC catalysis. In type II heterojunctions (Fig. 2b.ii), the CB and VB of semiconductor 2 are lower than the corresponding band of semiconductor 1. The photogenerated holes in semiconductor 2 will be thermodynamically transferred to

semiconductor 1 and vice versa. This process brings a spatial separation of electron-hole pairs. Following this design, Kuila et al. prepared the Ce MOF/$BiVO_4$ type-II heterojunction [42]. The built-in electric field across the space charge region extended the lifetime of the charge carriers, and the n-n heterojunction showed superior photoelectrochemical catalytic performance in degrading several dyes [42].

The p-n junction is a special type-II heterojunction which contains one p-type and one n-type semiconductor. In a p-n heterojunction, an internal electric field at the p-n interface and a space charge region occur before light illumination, in order to achieve the Fermi level equilibrium of the system. Subudhi et al. fabricated cobalt titanate integrated UiO-66-$NH_2$ p-n junctions and obtained outstanding $H_2$ evolution performance (530.87 μmole/h) [43]. The p-n heterojunction showed excellent visible light responsive capacity and prolonged charger carrier lifetime.

To substantiate the presence and establishment of these heterojunctions, a detailed characterisation of their morphologies can be carried out through high-resolution transmission electron microscopy (TEM). The utilization of X-ray photoelectron spectroscopy (XPS) and DFT simulation serve to definitively ascertain the classification of the heterojunctions into Type I, Type II, or Type III. In order to discriminate between direct Z-scheme and Type II heterojunctions, a series of tests for reactive oxygen species (ROS) generation can be conducted. These tests encompass techniques such as electron spin resonance spectroscopy, photoluminescence spectroscopy, and UV–Vis spectroscopy [44]. Furthermore, the validation of p-n junction formation can be accomplished through the construction of a Mott-Schottky plot [45].

Type-II and p-n heterojunctions are efficient for improving electron-hole separation. However, it is clear in Fig. 2b that both the oxidation and the reduction reactions take place at the semiconductor with the relatively lower redox potential. The redox driving force of the system is reduced by the charge transfer. While in a Z-scheme heterostructure, the holes of semiconductor 1 and the electrons of semiconductor 2 recombine. The photogenerated electrons left in semiconductor 1 can participate in the reduction process and the holes in semiconductor 2 can be involved in the oxidation reaction. Theoretically, half of the electrons in the Z-scheme structure are wasted, yet the charge separation is promoted, and the redox ability is maintained. Askari et al. reported a $CuWO_4/Bi_2S_3$/ZIF-67 dual Z-scheme system, which was applied to Metronidazole (MTZ) and Cephalexin (CFX) degradation with maximum photodegradation efficiencies at 92.5% and 87% [46]. The elevated photocatalytic capacity comes from a larger specific surface area from ZIF-67, lower band gap energy and efficient charge transfer from the formation of the dual Z-scheme heterojunction [46].

*Conductivity*

According to the structure of the MOFs, after binding of metal ions and organic linkers, generally there will be no free charge carriers left and no low-energy pathways available for charge transport. Thus, the majority of MOFs behave as insulators (conductivities < $10^{-10}$ S·cm$^{-1}$) [23]. Some common strategies have been reported to achieve suitable conductivities, including the usage of specific conductive organic linkers, the addition of guest dopants, and hybridization with conductive polymers or other graphene- or carbon nanotube-based materials [47].

Within the MOF-semiconductor system, the conductivity of the hybrid can be elevated by reducing the charge transport pathway in MOFs, typically by minimising the size of the MOFs. One of the most effective strategies is to coat a thin layer of MOF on the semiconductor substrate. Cui et al. fabricated a NiFe-MOF/$TiO_2$ heterostructure with a 1–2 nm of NiFe-MOF shell over the $TiO_2$ nanorods and reported 3.35-fold increase of photocurrent density at 1.23 V (*vs.* RHE) comparing to $TiO_2$ sample [48]. Improved charge injection and separation, as well as better stability, were obtained. Owing to the ultrathin MOF layer, photogenerated charge carriers could readily migrate to the surface for redox reactions. In addition, the thin and porous structure of NiFe-MOF does not block light absorption and mass transfer to $TiO_2$.

*Stability and pH of solvents*

The high specific surface area and porous structure of MOFs offer them great advantages in gas storage and separation. However, these unique properties also cause problems such as instability. While PC and PEC catalytic reactions are generally performed in aqueous solutions, it has been reported that MOFs could collapse after removing solvents on account of the capillary force [49]. Solvents with low surface tension could be applied to mitigate this problem. In MOF/semiconductor hybrid systems, the key factor that affects the stability is the pH of the electrolyte. The pH stability of several MOFs are shown in Fig. 2c [50]. In contrast, some common oxide semiconductors have wider ranges of stability for PC and PEC catalysis., ZnO is stable in electrolyte over a pH range from 9 to 13. $Fe_2O_3$ is stable in basic solution, while $WO_3$ is stable in acidic conditions [50]. Therefore, for hybrids electrolytes with a suitable pH range should be selected to ensure both MOF and semiconductor are stable during PC and/or PEC catalysis. During PEC measurements, hole-sacrificial agents like inorganic sodium sulfite or organic triethanolamine (TEOA) have been used to consume the photogenerated holes at the surface. The interaction between these agents and the MOFs should also be taken into account.

*Product selectivity*

HER and $CO_2$ reduction reaction are two most desired reactions occurring at the PEC photocathodes. As listed in Table 1, $CO_2$ could convert to CO, $CH_4$ etc. at similar potentials. Since the redox potential of popular photosensitisers like $[Ru(bpy)_3]^{2+}$ (−0.81 V *vs* SCE) is sufficiently negative for both the hydrogen evolution reaction and $CO_2$ to CO reaction, the MOF in the MOF/semiconductor hybrids must be selective [51]. For $CO_2$ reduction, HER becomes a side reaction and should be sup-

**TABLE 1**

**Redox potentials for $CO_2$ reduction reactions in aqueous at pH 7 [50].**

| | |
|---|---|
| $CO_2 + 6H_2O + 8e^- \rightarrow CH_4 + 8OH^-$ | −0.246 |
| $CO_2 + 5H_2O + 6e^- \rightarrow CH_3OH + 6OH^-$ | −0.399 |
| $CO_2 + H_2O + 2e^- \rightarrow CO + 2OH^-$ | −0.521 |
| $CO_2 + H_2O + 2e^- \rightarrow HCOO^- + OH^-$ | −0.665 |
| $2H_2O + 2e^- \rightarrow H_2 + 2OH^-$ | −0.414 |

pressed. It is reported that the incorporation of uncoordinated functional groups such as —F, —$NH_2$, —COOH can improve the selectivity and adsorption of MOFs for $CO_2$ reduction [15]. Besides, specific metal nodes like Co and doping with extra Ag NPs have been reported to enhance the selectivity of $CO_2$ reduction [52,53]. Investigations of $CO_2$ reduction and mechanisms will be discussed in sub-section 'Photocatalytic and photoelectrochemical $CO_2$ conversion'.

*Fabrication*

With careful design, MOF-semiconductor heterostructures can be fabricated with excellent performance. Generally, two strategies termed "ship in a bottle" and "bottle around the ship" have been established [52,53]. With the "ship in a bottle" method, MOF nanoparticles grow around semiconductors. MOFs and semiconductors are usually connected by coordination bonds and electrostatic interaction. Jin et al. modified $TiO_2$ with amino-MIL-125(Ti), and the structure performed well in PEC detection of the herbicide clethodim [54]. The latter selects MOF nanoparticles as the matrix and decorating guest particles. Xu's group decorated UiO-66 with CdS NPs and obtained superior $H_2$ production activity [55].

### *Advantages and limitations of MOF-semiconductor structures*

Incorporation of MOFs into traditional oxide semiconductors has several advantages including: (i) high porosity, which renders more active sites exposed and makes mass transport easier for surface redox reaction; (ii) light harvesting, as MOFs can be readily functionalised to absorb light over a relatively broad range; (iii) surface engineering, as MOFs can cover some structural defects which act as hole traps on semiconductor surfaces, and mitigate electron-hole recombination [56]. These types of MOF-semiconductor structures still exhibit some challenges, such as low charge transfer efficiency between MOF and semiconductors, poor stability, inadequate PEC performance, *etc*. Coupling plasmonic structures to MOF/semiconductor hybrid systems is an exciting strategy to enhance PC and PEC activities and has proved particularly promising in extending the light absorption range of MOF, semiconductor, and MOF/semiconductor hybrid photoelectrodes [57]. In addition, plasmonic nanostructures could also improve charge separation of MOFs and semiconductors, respectively, and increase the internal charge transfer efficiency between MOFs and semiconductors for MOF/semiconductor hybrid systems.

### *Fundamentals of plasmonic effect*

Pure metal in an external electromagnetic field can be described using the Drude model in which the conduction electrons of the metal are treated as a free electron gas, whilst the positive ions are fixed [58]. The electromagnetic waves can propagate in the metal and generate collective oscillation at the plasma frequency. The plasma frequency determines the permittivity of the metal. The collective oscillation is termed a volume plasmon. Furthermore, at the metal-dielectric interface, the excitation after illumination generates a surface plasmon resonance (SPR). The surface plasmon resonance has two modes, *i.e.* surface plasmon polaritons (SPP) and localised surface plasmon resonance (LSPR) (Fig. 3a.i). The collective oscillation of free electrons near the dielectric-metal interface is also termed as surface plasmon [59]. An SPP consists of an electromagnetic wave propagating along the interface in the air and charge motion which will be evanescently confined in the metal along the perpendicular direction [58].

The characteristic SPP resonance wavelength (λ) is given by *Eq.* (4.1) below:

$$\lambda = \frac{a}{\sqrt{i^2 + j^2}} \times \sqrt{\frac{\varepsilon_d \times \varepsilon_m}{\varepsilon_d + \varepsilon_m}} \tag{4.1}$$

where $a$ accounts for the periodic distance of the thin film, $\varepsilon_m$ and $\varepsilon_d$ are the permittivity of the metal and dielectric, respectively. Parameters $i$ and $j$ are wave vector indicators at the plane which determine the SPP resonance mode. The incident transverse-polarised wave couples to the SPP to generate a transverse-magnetic polarisation and a periodically changing surface charge density distribution, as shown in Fig. 8a. The electric field exponentially decays to different penetration depths in the surrounding media. The penetration depth of the evanescent field in the metal can be several nanometres, while the penetration depth of the evanescent field in the dielectric ranges from hundreds of nanometres to one micrometre. The surface plasmon propagation length $\delta_{SPP}$, with values from several micrometres to millimetres, is inversely proportional to the depths mentioned above [61]. In contrast, if the dimension of the interface is much less than $\delta_{SPP}$, the surface plasmon will be localised. Take metal nanoparticles as an example, an incident electromagnetic field with specific frequency causes oscillation of the free electrons, generating an oscillation of polarised charges and building a local electromagnetic field over the metal surface, as shown in Fig. 3a.ii. The resonance between the local electromagnetic field and external field is termed as LSPR.

The localised (dipole) surface plasmon frequency can be calculated using Eq. (4.2):

$$\omega_{LSPR} = \frac{\omega_p}{\sqrt{1 + 2\varepsilon_d}} \tag{4.2}$$

where $\omega_p$ is the plasma frequency, $\varepsilon_d$ is the dielectric permittivity. As the LSPR frequency of metal materials can be tailored by the size, morphology, and permittivity, it is feasible to design nanostructures with defined LSPRs.

The time scales of plasmonic energy transfer are shown in Fig. 3b. After collective electron oscillation, the plasmon resonance energy could dissipate within 20–30 fs via radiative photon re-emission and nonradiative decay. In the nonradiative mode, electron-hole pairs are excited in the metal. The plasmon energy transfers to individual hot carriers in the metal via Landau damping in 100 fs [62]. Exceptionally, in direct hot electron injection (HEI), the hot carriers occur in the semiconductor. After Landau damping, the majority of the energy dissipates via electron–phonon scattering within 100 fs–1 ps [58]. Alternatively, hot carriers excited in the metal could be transferred to semiconductors in the indirect HEI process before relaxation. Finally, hot carriers will fall to the fermi level and release heat in 1 ps–10 ns.

### *Mechanistic study of plasmonic enhancement*

SPP and LSPR give rise to near-field electromagnetic fields in the dielectric and metal. As the generation rate of energetic charge carriers is proportional to $|E|^2$, the electron-hole pair generation is therefore increased exponationaly [63]. Herein, for a metal–semiconductor junction, the plasmon energy must be higher than the bandgap energy of the semiconductor. Plasmonic energy can be transferred to a semiconductor through three main mechanistic pathways: (i) plasmon-induced resonance energy

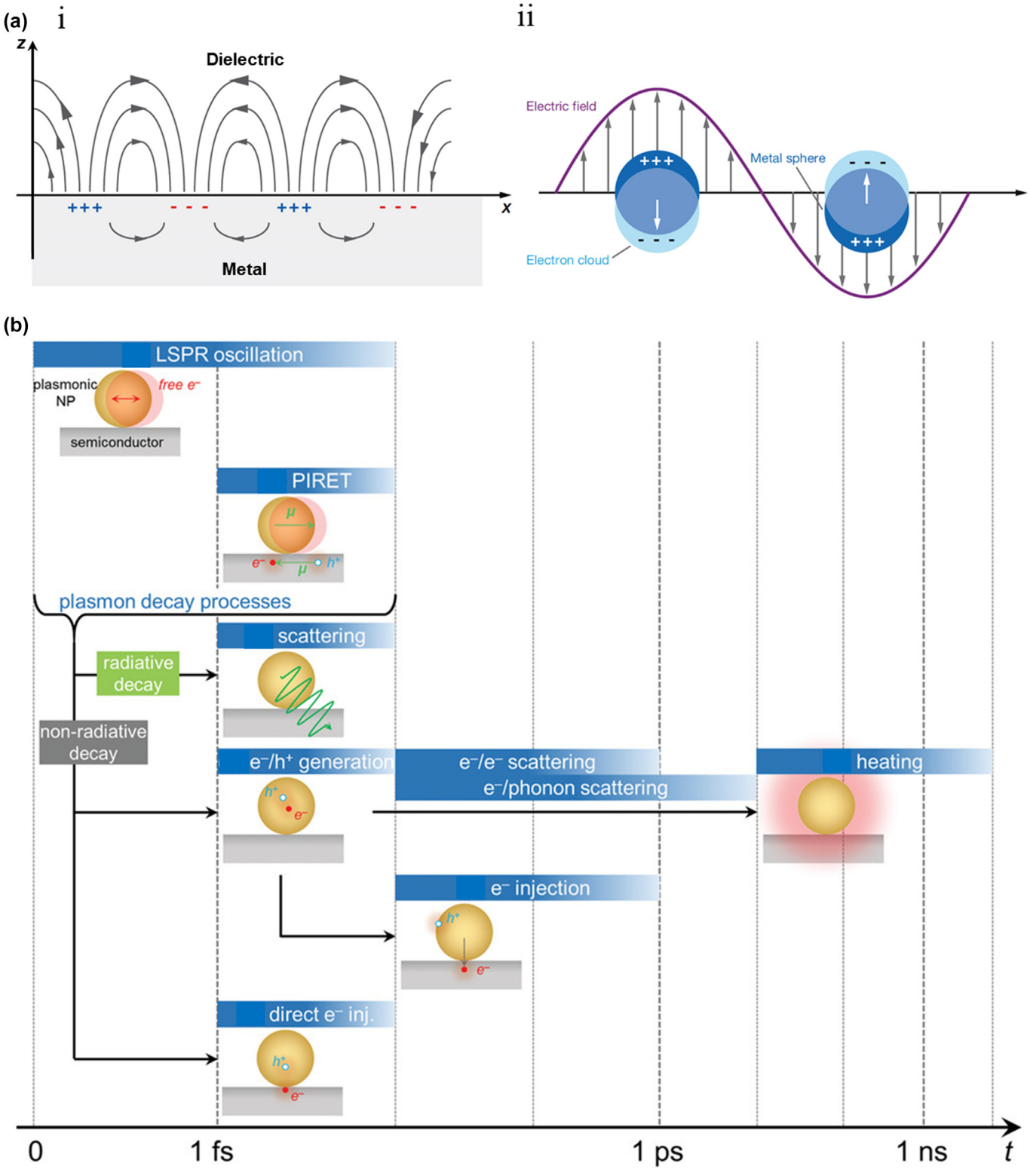


**FIG. 3**

(a) Schematics of (i) SPP and (ii) LSPR [60]. (b) The time scales of plasmonic energy transfer [58]. Reproduced with permission from [58,60]. Copyright IOP, 2018. Copyright John Wiley & Sons, 2019.

transfer (PRIET); (ii) light scattering/trapping; (iii) hot electron injection (HEI).

PIRET is a process that transfers energy from the plasmon to the semiconductor through the electromagnetic field generated by surface plasmon resonance or a dipole–dipole interaction. After the generation of surface plasmon dipoles, the dipoles can relax and excite electron-hole pairs in semiconductors. Local electromagnetic fields can non-radiatively excite interband tran-

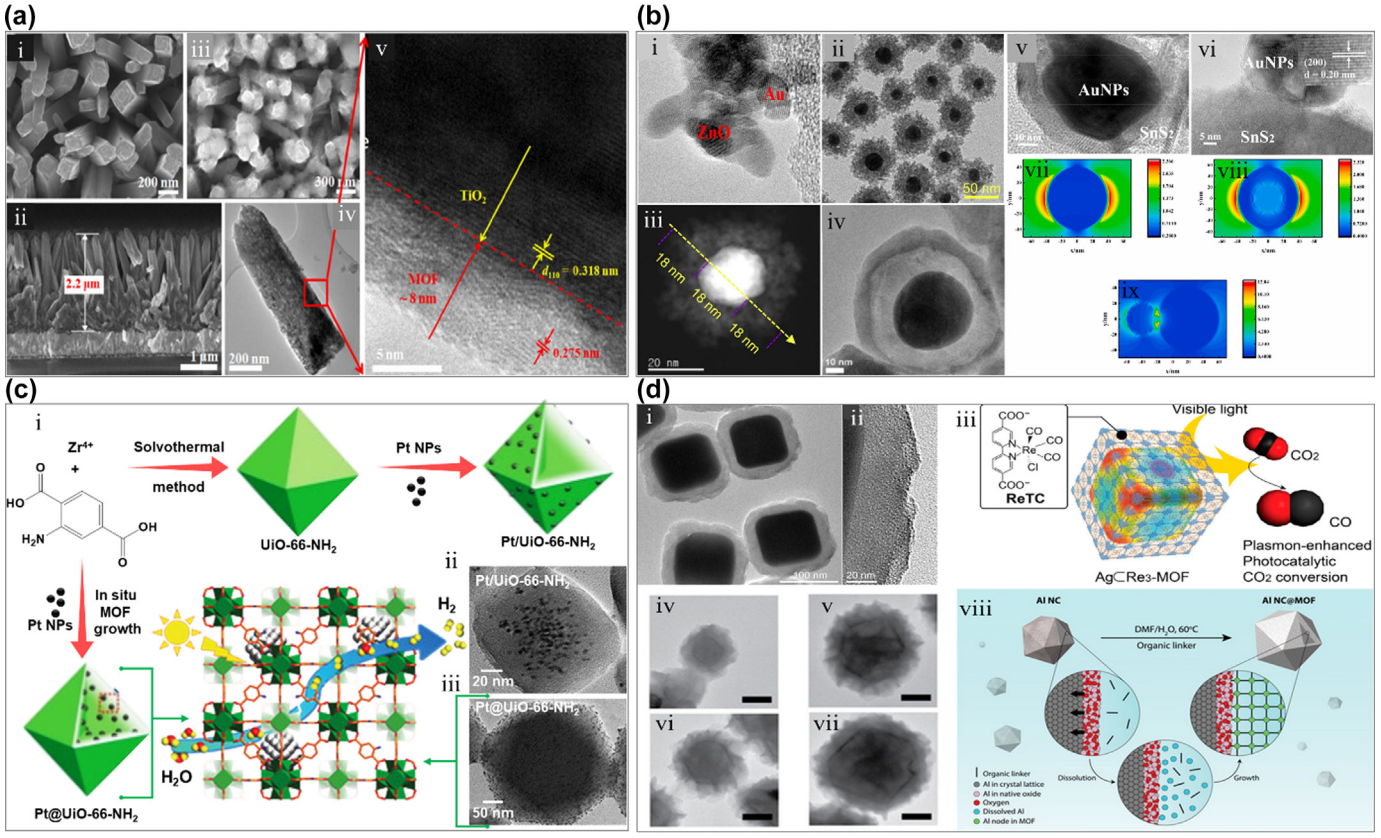


**FIG. 4**

(a) Microstructure of the $TiO_2$@MOF nanorod array. i. Top-view SEM image of $TiO_2$ nanorod array; ii. cross-section SEM image of $TiO_2$ nanorod array; iii. top-view SEM image of $TiO_2$@MOF nanorod array; iv. TEM and v. HRTEM images of a $TiO_2$@MOF nanorod [45]. Reproduced with permission from [45]. Copyright Springer Nature, 2018. (b) i. HRTEM of Au-ZnO, ii. TEM image of Au@$CeO_2$ core–shell NPs, iii. high-resolution dark filed TEM image of an Au@$CeO_2$ core–shell structure, vi. High-magnification TEM image of an Ag-CdS Yolk/Shell heterostructure, v. TEM image of the $SnS_2$@AuNPs core–shell structure; vi. TEM image of the $SnS_2$@AuNPs Janus structures, vii-ix. The near field distribution of $SnS_2$ nanoparticle, the core–shell structure and the Janus structure with AuNP. Reproduced with permission from [76–79]. Copyright John Wiley and Sons, 2021. Copyright Elsevier, 2021. Copyright John Wiley and Sons,2021. Copyright Elsevier, 2021. (c) TEM images of i. Synthesis process and hydrogen production schematic of Pt-UiO-66-$NH_2$, ii. Pt@UiO-66-$NH_2$ and iii. Pt/UiO-66-$NH_2$,. Reproduced with permission from [87]. Copyright JOHN/WILEY & SONS, 2016. (d) TEM images of i. Ag ⊂ $Re_3$-MOF and ii. Magnified TEM image of $Re_3$-MOF, iii. Structures of Ren-MOF and Ag ⊂ $Re_n$-MOF for plasmon-enhanced photocatalytic $CO_2$ conversion. Al NC@MIL-53(Al) with nominal Al core sizes of iv. 50 nm, v. 85 nm, vi. 110 nm, and vii. 150 nm. Viii. Synthesis of Al NC@MOF plasmonic heterostructure based on dissolution-and-growth. Reproduced with permission from [88,89]. Copyright American Chemical Society, 2017. Copyright American Association for the Advancement of Science, 2019.

sitions in the semiconductor. PIRET is a blue-shifted energy transfer process, and can lead to absorption of light with energy below the semiconductor bandgap. Its efficiency is affected by the distance between the metal and semiconductor, and the spectral overlap between the plasmon resonance band and the semiconductor absorption region [62]. Unlike HEI, direct contact between the semiconductor and plasmon nanoparticle is not required.

As mentioned above, LSPR on metallic nanoparticles involves resonance between the external field and the local intense near-field electromagnetic field originating from the oscillation of free electron gas. The scattering and absorption cross-section are therefore much larger than the spatial size of the metallic nanoparticles. When a semiconductor is integrated with the metallic nanoparticles, more incident photons are extracted by the metallic nanoparticles in the first step. Then the plasmon resonance process can dissipate energy via radiative decay, with energy transferred to the semiconductor through re-emission of photons. In general, the metallic nanoparticles should be larger than 50 nm in diameter, as the absorption cross-section is related to their dimension [62,64]. Unlike HEI and PIRET, the near-field excitation enhancement and light scattering could not extend the absorption range through the light spectrum.

HEI includes indirect electron transfer and direct electron transfer [65]. Physical contact between the metal and semiconductor is an essential requirement for HEI processes. After the resonant excitation, the plasmon resonance could dissipate in a nonradiative pathway to excite electron-hole pairs in the metal. Subsequently, hot carriers relax to a Fermi–Dirac distribution by electron–electron scattering within 1 ps [58]. Hot carriers with energy higher than the Schottky barrier at the metal–semiconductor interface could be directly injected into the conduction band of the semiconductor. The whole process is termed as indirect electron transfer. In this mode, the energy of hot electrons is not determined by incident light, which means photons with energy below the bandgap could be utilised, thereby expanding the spectral light absorption range, enabling lost photon (below the band gap of the semiconductor) harvesting. However, this

two-step process has relatively low theoretical maximum electron transfer efficiency (8%) [66]. In direct electron transfer, hot electrons are induced directly in the semiconductor in a chemical interface damping process [65]. In this case, the electron transfer efficiency could be much higher than that of the indirect mode [67].

## Plasmon enhanced MOF-semiconductor composite photocatalysts/PEC catalysts

### *Binary composite photocatalysts/PEC catalysts*

Investigations into semiconductor-MOF, plasmon-MOF and plasmon-semiconductor composite photoelectrodes have been reviewed by several research groups [68,69]. In this article, we briefly summarise these binary hybrid photoelectrodes.

#### *MOF-semiconductor composites*

MOF-semiconductor binary composites have been investigated for light-induced applications [70]. The encapsulation of visible light responsive MOF with wide band gap semiconductors (*e.g.* $TiO_2$, ZnO) is a normal strategy in PEC cell or photocatalysts. The semiconductor and the chosen MOF with the same metal source are always the preferential combination because of better interface matching and convenience in fabrication. Xiao's group reported a facile route to synthesise amorphous $TiO_2$@$NH_2$-MIL-125(Ti) heterostructures [71]. The encapsulation of $NH_2$-MIL-125 (Ti) on $TiO_2$ could preserve $Ti^{3+}$ active species in the photocatalytic reaction. Meanwhile, $TiO_2$ could act as a platform for transferring photoinduced electrons from $NH_2$-MIL-125(Ti).

Binary composites consisting of the semiconductor and MOF with different metal elements have also been investigated. Yang et al. fabricated $TiO_2$@MOF core–shell nanorod array photoanodes with a photocurrent density of 2.93 mA $cm^{-2}$ at 1.23 V *vs.* RHE (Fig. 4a) [45]. $TiO_2$ and Co-MOF formed a p-n junction, which improved the charge separation in $TiO_2$ nanorods. The novel vertically aligned core–shell structure renders a longer optical pathway with a shorter distance for holes diffusing from $TiO_2$ to the electrolyte.

Jia et al. developed ZnO@ZIF-8/67 photoanodes and exhibited a 9.2 times increase in light current density (0.11 mA $cm^{-2}$ at 1.23 V *vs.* RHE) compared to the pristine ZnO nanorod arrays [72]. The integration of ZIF-67 simultaneously extended the light harvesting spectrum to the visible-light range and suppressed the charge recombination.

Several studies have been made based on hematite. Jiang's group incorporated MIL-53(Fe) microrods with $Fe_3O_4$ nanospheres *via* a simple one-pot solvothermal process [73]. The synergistic effect brought enhancement both in PEC water oxidation and organic pollutant (RhB, PNP) photodegradation. Zhang et al. demonstrated an *in situ* growth of Co-MOF nanosheets on an hematite nanorod array and a photocurrent density of 2.0 mA $cm^{-2}$ at 1.23 $V_{RHE}$ was obtained [74]. The atomically distributed $Co^{2+}$ delivered outstanding hole storage capability and high charge transport efficiency.

In terms of $CO_2$ reduction, Crake et al. integrated $TiO_2$ nanosheets with $NH_2$-UiO-66 *via* an *in situ* growth and achieved capture and photocatalytic reduction of $CO_2$. The as-generated heterojunction of $TiO_2$ nanosheets and $NH_2$-UiO-66 showed high $CO_2$ uptake and prevented the aggregation of $TiO_2$. In this system, $NH_2$-UiO-66 acted as $CO_2$ adsorbent, charge separator, light transducer, as well as co-catalyst rendering more active sites for $CO_2$ reduction.

As to light-induced environmental remediation, Du et al. reported MIL-100(Fe)@g-$C_3N_4$ heterojunctions from ball-milling and annealing, which demonstrated promising photocatalytic performance for Cr(VI) reduction and organic pollutant degradation under the sunlight [75]. The enhanced Cr(VI) reduction arised from effective photoexcited electron transfer from g-$C_3N_4$ to MIL-100(Fe). This work implied the potential of MOF and economic semiconductor for contamination treatment.

#### *Plasmon-semiconductor composites*

In terms of plasmon-semiconductor photoelectrodes, common structures include: semiconductors decorated with plasmonic nanocrystals, plasmonic metal–semiconductor core–shell structures, Yolk/Shell and Janus plasmonic metal–semiconductor strucutures [69]. Yasmeen et al. decorated ZnO nanoparticles with Au nanospheres and the photocatalytic degradation capacity was improved, shown in Fig. 4b.i [76]. Dao et al. prepared plasmonic Au@$CeO_2$ core–shell structure with diameter of ~60 nm for photocatalytic HER (Fig. 4b.ii–iii). The LSPR was excited on Au and the charge carrier generation rate of $CeO_2$ was elevated [77]. Jung et al. fabricated Ag-CdS Yolk/Shell heterostructures and obtained superior photocatalytic HER performance compared to CdS hollow nanoparticles, which could be attributed to the energy transfer from Ag to CdS and a light-matter interactions in the yolk-shell nanostructure [78] (Fig. 4b.iv). Fu et al. explored $SnS_2$@-AuNPs Janus heterostructures and reported that the Janus structures showed better LSPR property than the core–shell $SnS_2$-Au NPs (Fig. 4b.v–vi). The latter delivered minor photocatalytic enhancement. As shown in Fig. 4b.vii–ix, prominent optical field enhancement of *ca.*12-fold was calculated at the edge between Au and $SnS_2$, while the core–shell structure presented no significant enhancement (~2 times) [79].

Apart from water splitting, $TiO_2$ and ZnO were also applied to photo-induced antibacterial activities. O. Akhavan et al. fabricated Ag-$TiO_2$/Ag/a-$TiO_2$ nanocomposite films for the photodegradation of Escherichia coli bacteria under visible light, while Mao et al. prepared Ag/Ag@AgCl/ZnO hybrid nanostructures embedded into hydrogel for wound healing acceleration [80,81]. In both systems, semiconductors produced photogenerated reactive oxygen species (ROS). Silver nanoparticles provided LSRP and the release of silver ions contributed to the enhanced antibacterial activity. The Ag-$TiO_2$/Ag/a-$TiO_2$ nanocomposite exhibited a controlled ion releasing process by interdiffusion of molecular $H_2O$ and Ag nanospheres through pores of the films. For Ag/Ag@AgCl/ZnO, a boost of ROS resulted in the enhancement of photocatalytic and antibacterial performance, compared with ZnO. The hydrogel system offered controllable and sustained release of $Ag^+$ and $Zn^{2+}$. These two ions conducted a synergistic antibacterial effect against Escherichia coli and Staphylococcus aureus, and accelerated wound healing.

Apart from LSPR plasmonic metal nanocrystals, other plasmonic nanostructures like nanohole arrays enable SPP mode plasmonic enhancement. Wu's group exploited gold nanohole arrays to generate both SPP and LSPR simultaneously. The energy

of SPP and LSPR were transferred to hematite nanorods dominantly *via* PIRET and a more than 10-fold enhancement was observed in the incident photon to current efficiency (IPCE) spectrum [82]. SPP mode exploitation was also reported in plasmon/MOF composites for sensing and plasmon/semiconductor hybrids for PEC catalysis [82–84].

*Plasmon–MOF composites*

The Plasmonic-MOF composites are another research hot topic and have been intensively researched in applications such as biosensing, drug delivery and catalysis [85,86]. Typical heterostructures are MOFs decorated with plasmonic NPs and metal nanoparticle-MOF core–shell structures. Xiao et al. fabricated Pt@UiO-66-$NH_2$ structures, shown in Fig. 4c, *via* a solvothermal method with pre-prepared Pt NPs and precursor solution of UiO-66-$NH_2$ [87]. In comparison with Pt/UiO-66-$NH_2$ (Fig. 4c.ii), internal Pt NPs shortened the electron transport route to the UiO-66-$NH_2$. The Pt NPs also suppressed the charge recombination and the porous structure of UiO-66-$NH_2$ did not block the mass transfer of photocatalytic HER.

Choi et al. reported Ag-MOF heterostructure for $CO_2$ reduction [88]. The $Zr_6O_4(OH)_4(—CO_2)_{12}$ was functionalised with $H_2$-ReTC and $H_2$BPDC to form $Re_n$-MOFs. A $Re_n$-MOF coating layer with thickness of 16 and 33 nm could be generated on the surface of Ag nanotubes via vigorous stirring for specific reaction times (Fig. 4d.ii). The silver core at the centre could provide an enhanced electromagnetic field to improve the overall photocatalytic performance. The modified $Re_n$-MOFs shell rendered numerous active sites and high porosity for mass transfer.

Robatjazi et al. reported the growth of MOF shell surrounding Al nanocrystals (Fig. 4d.viii). During the growth of the MOF layer, Al was oxidised to $Al^{3+}$ and served as the metal nodes for MIL-53(Al). The MOF layer improved the photocatalytsis of Al nanocrystals for hydrogen–deuterium exchange and reverse water–gas shift reactions [89].

### *Ternary plasmon-MOF-semiconductor hybrid photocatalysts/ PEC catalysts*

To date, there are few papers reporting ternary plasmon/MOF/semiconductor composites, based on LSPR effect, for photocatalysis or photoelectrochemical catalysis [90–92]. Cui et al. grew $NH_2$-MIL-125 thin film on $TiO_2$ nanorod array, and further decorated silver NPs onto the $NH_2$-MIL-125 thin film, as shown in Fig. 5a–j. The schematic of Ag/$NH_2$-MIL-125/$TiO_2$ photoanode for PEC water splitting is presented in Fig. 5k–l. The photocurrent density at 1.23 V (*vs*. RHE) was enhanced by 4.42 times [90]. The IPCE value at 390 nm increased to 51%, and high charge injection and separation efficiency was obtained [90]. The IPCE did not increase below the band edge of $TiO_2$, which excluded the blue-shift PIRET effect. Since the *in situ* implanted Ag nanoparticles only had a diameter of around 10 nm, the light trapping effect was limited. Considering the hot electron injection mode, the hot electrons generated in silver have to first hop to $NH_2$-MIL-125, and then transfer to the $TiO_2$. This process was suggested to be less efficient. Even though, the IPCE data showed dramatic enhancement around 400 nm, which could be attributed to localised near-field electromagnetic field enhancement to promote electron-hole pair excitation in $NH_2$-MIL-125 and $TiO_2$. HEI also plays a minor role in the enhancement. Additionally, $NH_2$-MIL-125 provided a wider light absorption compared with bare $TiO_2$. Similar to the LSPR effect from plasmonic Ag NPs, the heterojunction between $NH_2$-MIL-125 and $TiO_2$ facilitated efficient charge separation.

Theoretically, plasmonic metal nanoparticles encapsulated in between the MOF and semiconductor should result in more efficient near-field electromagnetic field enhancement and HEI. Dou et al. prepared a ZIF-67/Metal NPs/ZnO composite photoelectrode [91], as shown in Fig. 6c. A six-fold photocurrent density enhancement was obtained compared to the bare ZnO photoanode. Au NPs of diameter 15 nm could not bring a significant light trapping effect (Fig. 6a–b). As the Au NPs were placed at the interface between ZnO and ZIF-67, the localised near-field electromagnetic field equally affected the ZnO and ZIF-67. Porous ZIF-67 did not block the light penetration into the Au NPs and ZnO. Therefore, once hot carriers were excited in Au NPs, they could directly overcome the Schottky barrier and inject into ZnO. The absorption peak of Au NPs did not match well with the band edge of ZnO, so PIRET was considered to be ineffective in this process. The performance enhancement from plasmonic effect can be attributed to HEI and near-field electromagnetic field enhancement. The visible-light responsive ZIF-67 contributed to elevated performance through broad light harvesting, a porous structure for mass transport and abundant active sites for surface redox rection.

Butburee et al. prepared hybrid photocatalysts which contained ZIF-8/AuCu nanoprism/$TiO_2$ junction [92] (Fig. 6f). Finite Different Time Domain (FDTD) modelling was applied in this work and predicted an electric field enhancement at 586 nm at the metal/semiconductor interface. The nanoprimes had sides of ~100 nm (Fig. 6d–e), the light trapping became a significant mechanism for plasmonic enhancement. A large cross section of energy flux was captured and utilised by the metal NPs, and the energy was further transferred to the semiconductor by re-emission of photons without energy loss. Besides, the metal nanoprism also acted as a bridge to facilitate charge transport between the ZIF-8 and $TiO_2$. As a cocatalyst, the porous ZIF-8 provided many $CO_2$ adsorption sites for efficient $CO_2$ reduction.

Xie's group fabricated the α-$Fe_2O_3$@Ag@ZIF-67 ternary composite photoanode (Fig. 7) [57]. Visible light responsive ZIF-67 improved the light harvesting. The Ag nanorods were functionliased with PEG-ligand which hindered the direct hot electron transfer. FDTD was applied to simulate the local electomagnatic field and far-field spectra of Ag nanorods. The Ag nanorods in the study had a dominant absorption cross-section and a less strong light scattering effect. The resonance peaks of silver nanorods with different aspect ratios were calculated with FDTD and measured with UV–Vis. They invetisgate the plasmonic enhancement mechanism via tailing the optical properties of Ag nanorods with different aspect ratios and reported that PRET dominated the plasmonic energy transfer from Ag to α-$Fe_2O_3$ and ZIF-67 in this system.

On the other hand, several MOF-semiconductor-plasmonic enhanced ternary photocatalysts have been reported. Feng et al. preapred ternary UiO 66/g $C_3N_4$/Ag composite photocatalysts and applied them in the degradation of contaminants like Rhodamine B [93]. The addition of g $C_3N_4$ and silver improved

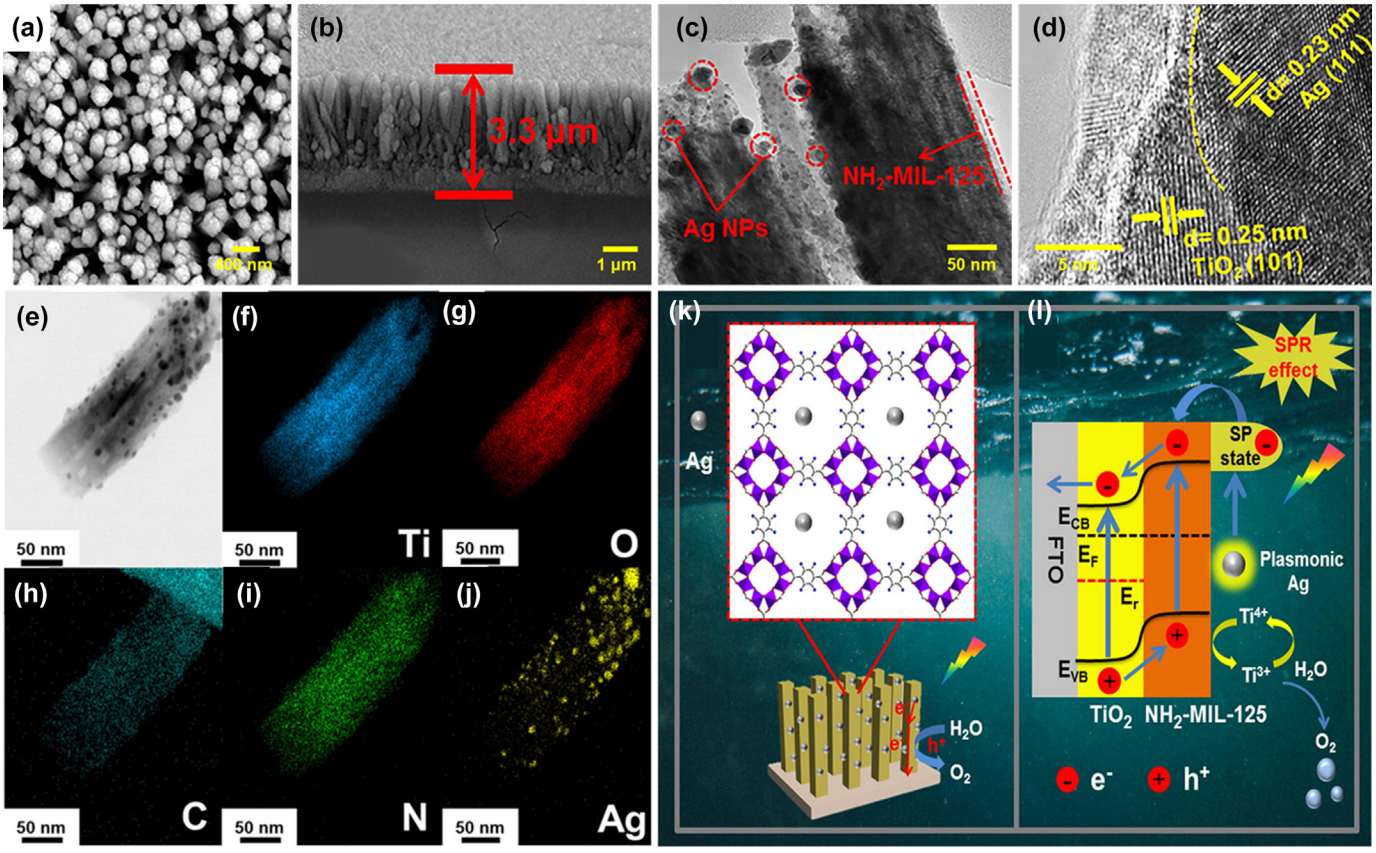


**FIG. 5**

(a-b) SEM images of Ag/$NH_2$-MIL-125/$TiO_2$. (c-d) TEM images of Ag/$NH_2$-MIL-125/$TiO_2$. (e-j) STEM images of Ag/$NH_2$-MIL-125/$TiO_2$, (k-l) Schematic of Ag/$NH_2$-MIL-125/$TiO_2$ photoanode for PEC water splitting. Reproduced with permission from [90]. Copyright Elsevier, 2020.

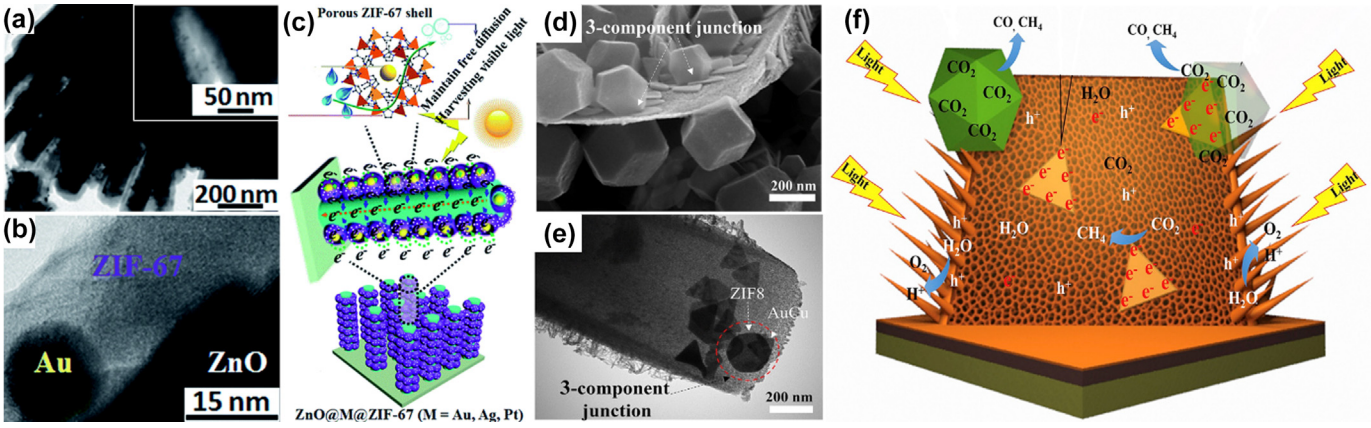


**FIG. 6**

TEM images of (a–b) ZnO@Au@ZIF-67, (c) ZnO@Au@ZIF-67 photoanode for PEC water splitting, (d–e) $TiO_2$-ZIF-8-AuCu. (f) $TiO_2$-ZIF-8-AuCu for $CO_2$ photocatalytic reduction, Reproduced with permission from [91–92]. Copyright Royal Society of Chemistry, 2017. Copyright Elsevier, 2019.

the light absorption, charge separation and mobility, thereby elevating the photocatalytic capability. Similar to PEC photoelectrodes, design of the semiconductor-MOF-plasmonic metal NP system can improve the performance. Several plasmonic enhanced ternary photocatalysts with novel structures are shown in Fig. 8. Wang et al. dispersed CdS coated gold nanoparticles into MIL-101 (Cr) and studied photocatalytic HER (Fig. 8a–c) [94]. The porous MIL-101 (Cr) provided abundant active sites and harvested photons while Au@CdS created LSPR, accelerated the charge transfer and broadened the light absorption of CdS. Furthermore, the semiconductor/plasmonic NP hybrids can be encapsulated into the MOF nanocrystals. Sofi et al. prepared HKUST-1@Ag-$Ag_3PO_4$ heterostructures and characterised the photocatalytic performance by degradation of PBS [95]. The LSPR from Ag NPs and Z-scheme energy transfer provided a superior photocatalytic performance for the system. As can be seen from Fig. 8f, electrons excited in $Ag_3PO_4$ could be collected by silver NPs while holes in $Ag_3PO_4$ could directly transfer PBS to $CO_2$

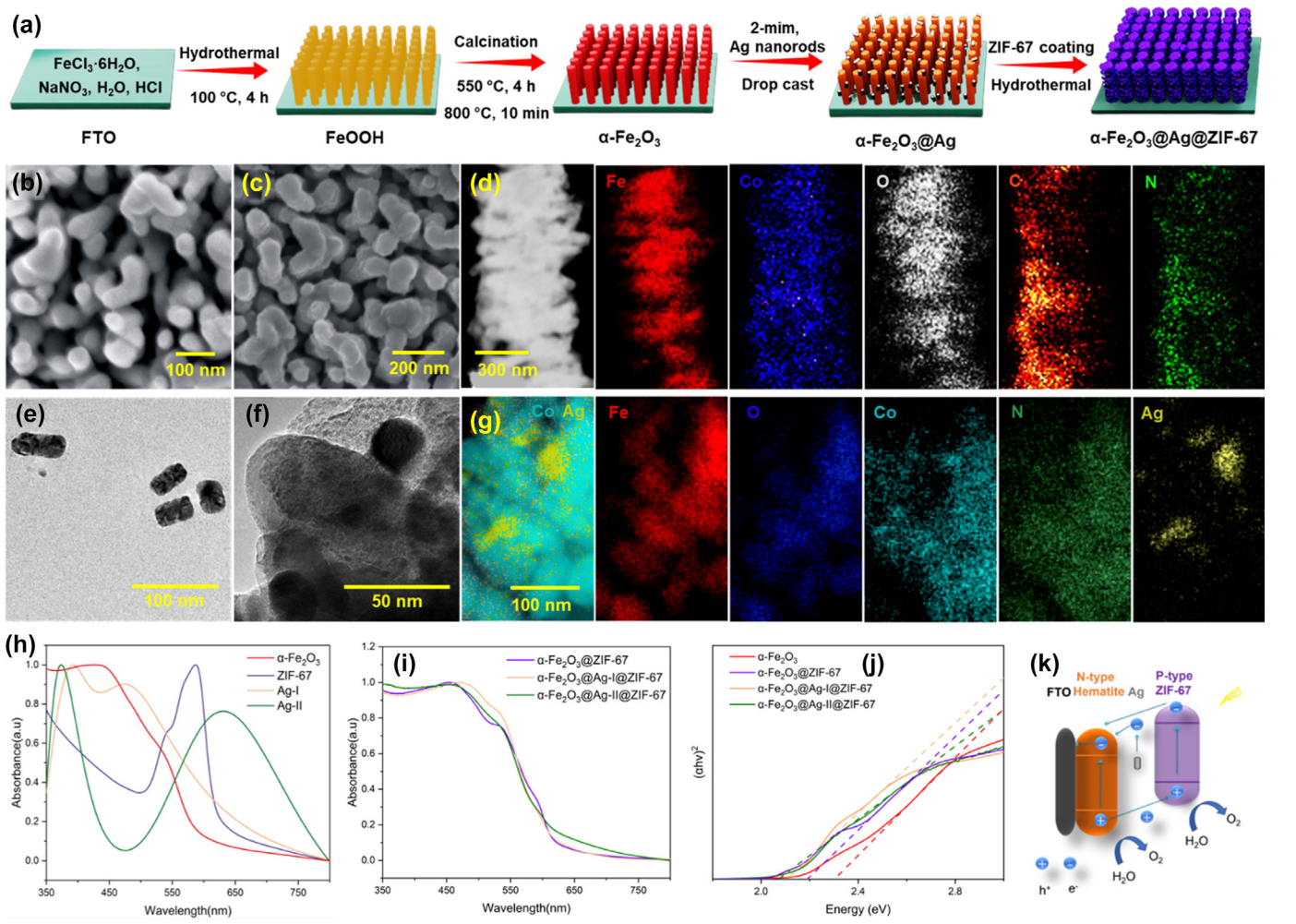


**FIG. 7**

(a) Scheamtic of workflow of α-$Fe_2O_3$@Ag@ZIF-67 photoanode for PEC water splitting. SEM images of (b) α-$Fe_2O_3$ (c) α-$Fe_2O_3$@ZIF-67. (d) STEM images of α-$Fe_2O_3$@ZIF-67. TEM images of (e) Ag nanorods (I), (f) α-$Fe_2O_3$@Ag@ZIF-67. (g) STEM images of α-$Fe_2O_3$@Ag@ZIF-67. (h) Normalised UV–Vis spectra of α-$Fe_2O_3$, ZIF-67, Ag-I, Ag-II. (i) UV–Vis spectra of α-$Fe_2O_3$@ZIF-67, α-$Fe_2O_3$@Ag-I@ZIF-67, α-$Fe_2O_3$@Ag-II@ZIF67. (j) Tauc plots of α-$Fe_2O_3$, α-$Fe_2O_3$@ZIF-67, α-$Fe_2O_3$@Ag-I@ZIF-67, α-$Fe_2O_3$@Ag-II@ZIF67. (k) Schematic of charge carrier and reaction pathway of a-$Fe_2O_3$@Ag@ZIF-67. Reproduced with permission from [57]. Copyright Elsevier, 2023.

and $H_2O$. Silver NPs therefore helped the effective charge separation of $Ag_3PO_4$. Moreover, Ag NPs provided hot electrons and transport to HKUST-1 and were involved in the photocatalytic oxidation process. Apart from all these structures, MOF and semiconductors can have the core–shell structures. Tilgner *el al.* reported the MIL-101 (Cr) core and gold/anatase shell photocatalyst for visible-light-driven wastewater purification [96]. The MOF core-crystalline anatase shell decorated with plasmonic gold NPs is presented in Fig. 8g–i. In addition to providing vast active sites, the MIL-101 (Cr) core also renders good stability of the whole system. Fig. 8i indicates how photogenerated electrons can transfer from gold to $TiO_2$ and participate in the photocatalytic reduction reaction.

## *Design consideration of plasmon-MOF-semiconductor photocatalysts/PEC catalysts*

### *Plasmonic metal*

The near-field enhancement and absorption cross-sections of various elements in the form of nanospheres have been studied, as shown in Fig. 9a and b [97]. It is clear that copper, silver and gold are good candidates as plasmonic materials. Moreover, for a particular metal, the absorption peak can be manipulated by nanostructuring. The absorption edge of Ag nanocubes red shifts as the cube size increases. Apart from nanocubes and nanospheres, other structures such as nanostars, nanoprisms can also bring excellent plasmonic enhancement. Notably, nanohole arrays give characteristic SPP and LSPR modes for enhancing performance by multiple pathways.

### *General strategies to constructure plasmon–MOF-semiconductor photoelectrodes*

The MOF-semiconductor composites have been discussed in detail in previous sections. When a plasmonic component is introduced, a "device-by-design" approach should be applied. As mentioned above, Cu, Ag and Au are all good candidates but Cu suffers from relatively poor stability. Other elements like Ru and Rd are less cost-effective. On the other hand, various structures such as MOF-semiconductor core–shell,

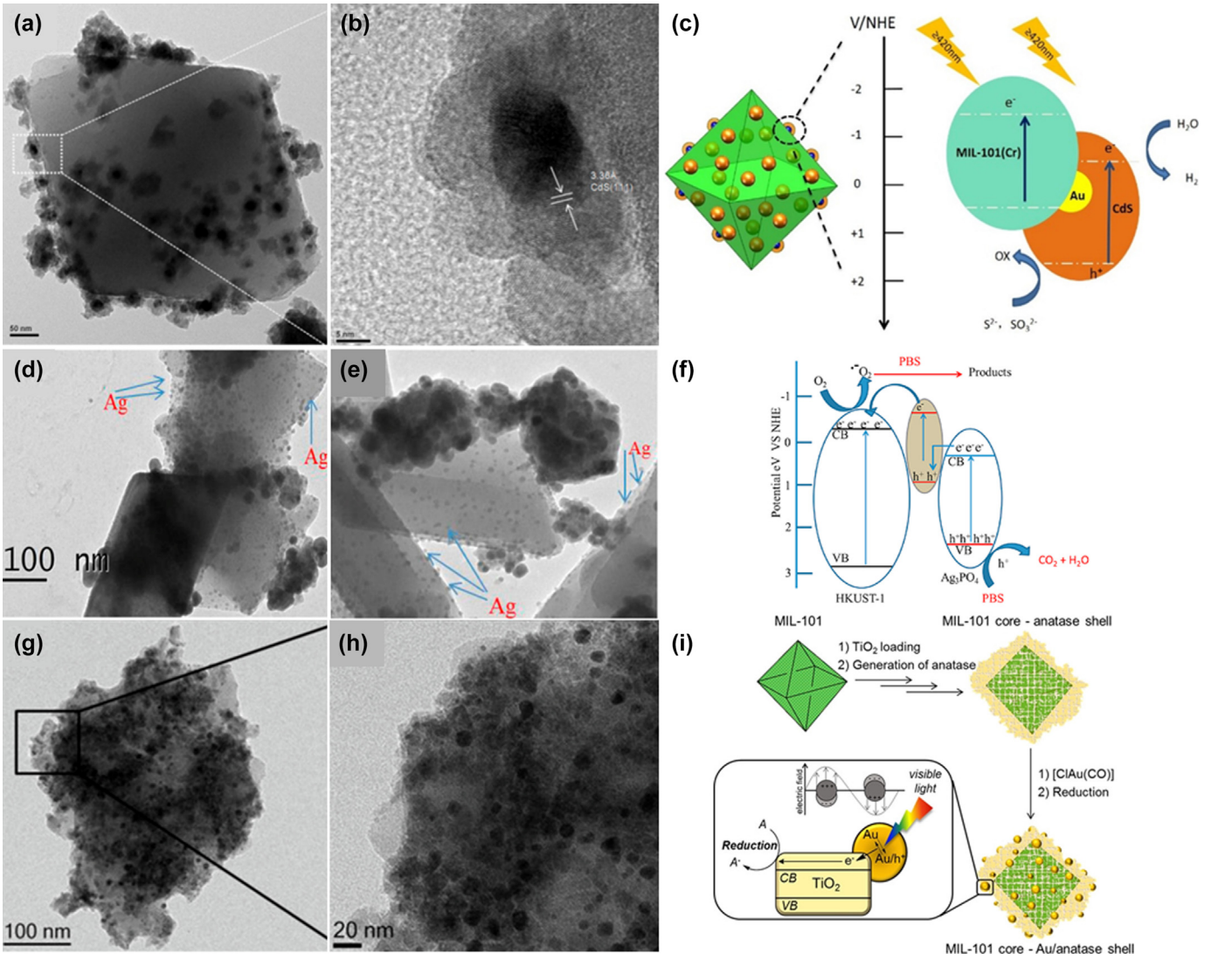


**FIG. 8**

(a–c) TEM images and Photocatalytic mechanism of UiO 66/g $C_3N_4$/Ag, (d–f) TEM images and schematic of Au@CdS/MIL-101 for photocatalytic HER, (g–i) TEM images and schematic of HKUST-1@Ag-$Ag_3PO_4$, (j–k) TEM images and schemiatic of fabrication process and photocatalysis of MIL-101-core–Au/anatase-shell compound. Reproduced with permission from [94–96]. Copyright Elsevier, 2016. Copyright Elsevier, 2018. Copyright John Wiley and Sons, 2017.

semiconductor-MOF core–shell, plasmon-semiconductor core–shell structures have been reported in ternary composite photoelectrodes. The structures of these three components deserves further investigation. In our opinion, MOF-plasmonic NP-semiconductor should be better than MOF-semiconductor-plasmonic NP structure, as plasmonic NPs at the interface could provide more effective near-field electromagnetic fields and hot electron transfer. The MOF could be either the core or outer layer as a framework to provide stability or as a cocatalyst to favour surface redox reaction, respectively.

Metal thin films could be exploited to take advantage of SPP modes. Ideally, the ternary composites should contain metal thin films and metal NPs to providing both SPP and LSPR modes, a sandwich-liked MOF-Plasmonic NP-Semiconductor structure with the light responsive MOF acting as both photosensitizer and co-catalyst should be made. In order to maximise various plasmonic enhancement pathways, the absorption peak of the plasmonic NPs should be precisely tailored with the band edge of the semiconductor and absorption band of the MOF.

It is noteworthy that the introduction of metallic NPs may not or not only bring plasmonic properties. For example, Pt NPs could build Schottky junctions with semiconductors to promote charge separation. Li et al. reported an Au/$Fe_2O_3$ photoanode [98]. The mismatch of the Fermi level of hematite and the gold work function induced electron transfer and band bending. The Au/$Fe_2O_3$ Schottky junction lead to band bending of the

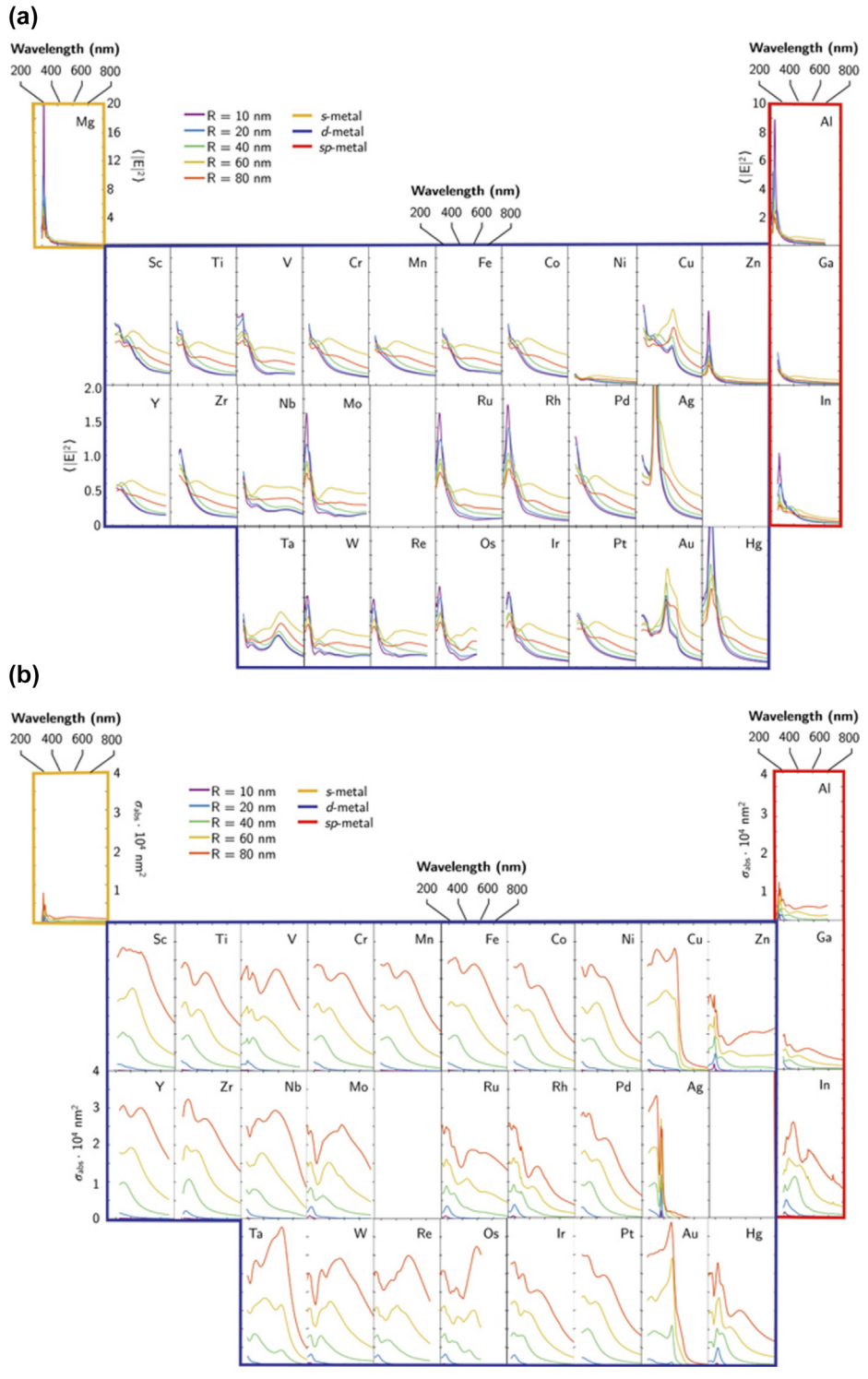


**FIG. 9**

(a) The near-field enhancement and absorption cross sections of different elements in the form of nanospheres [97]. (b) The absorption cross sections of different elements in the form of nanospheres [97]. Reproduced with permission from [97]. Copyright AIP, 2020.

CB and VB of hematite, thereby accelerating electron-hole pair separation and further improved the incident-photon-to-current-conversion efficiency. Besides, noble metal nanoparticles are catalytic for many reactions, which may bring enhancement to PC/PEC performance. The distribution position, dispersion state and surface charge state of metallic NPs also have significant impact on their plasmonic performance.

## Applications of plasmonic enhanced photocatalysts/PEC catalysts

MOFs with suitable HOMO and LUMO levels can fulfil catalytic functions, their high surface area giving good performance. In MOF/semiconductor hybrid systems, the distances between charges carriers and surface reaction locations are shortened.

Moreover, the recombination rate of electron – hole pairs is decreased drammtically [99,100]. However, most photocatalytic MOFs exhibit wide band gaps, which causes inferior light absorption efficiency, especially in the visible and near-infrared regions. Thus, the superior redox activity and high photocatalytic efficiency are difficult to realise [101,102]. plasmonic nanostructures can greatly enhance the PC and PEC activities due to plasmonic energy transfer from the metal nanostructure to MOF and/or semiconductor. Recently, researchers have reviewed binary structured photoelectrodes including MOF/semiconductor, semiconductor/plasmonic metal and MOF/plasmonic metal hybrid systems. In this review, only recent applications of ternary structured photoelectrodes (plasmonic metal/MOF/semiconductor) are considered in detail. The applications of the ternary systems include water splitting, $CO_2$ reduction and degradation of organic pollutants, as summarised in Table 2.

### *Photocatalytic and PEC water splitting*

To split water, photoelectrodes for both the HER and the OER processes are required. In this section, some examples of plasmonic enhanced HER and OER ternary photoelectrodes are reviewed. Wang et al. developed a ternary nanostructured heterojunction of Au nanoparticles, CdS and MIL-101 as a photocathode for HER catalysis [94]. Au NPs were highly dispersed on MIL-101 and CdS was coated on the Au NPs. In their research, the $H_2$ production rates of binary nanostructured photocathodes (CdS/MIL-101) with different MIL-101 concentrations were compared, shown in Fig. 10a. Compared with pure CdS, all the binary photocathodes had excellent enhancement of hydrogen generation rates and the highest rate they achieved was 208.2 $\mu molh^{-1}$/10 mg. The $H_2$ evolution rate of Au/CdS/MIL-101 was compared to the binary system, shown in Fig. 10b. The superior hydrogen generation rate of Au/CdS/MIL-101 can be observed with 250 $\mu molh^{-1}$/10 mg, which is 2.6 times larger than bare CdS. Moreover, the quantum efficiency of Au/CdS/MIL-101 achieved 8.8% at 420 nm, demonstrating the effective enhancement of $H_2$ evolution by incorporating Au NPs and MOF MIL-101. They further investigated the functions of Au or MIL-101, respectively. As shown in Fig. 10b, the Au/CdS/MIL-101 has a superior $H_2$ evolution performance than Au/CdS and

**TABLE 2**

**Photocatalytic performances of plasmonic MOF based photoelectrodes.**

| Number | Photocatalyst | Target reaction | Hydrogen production rate | Photocurrent density | Electrolyte in PEC measurement | Reference |
|---|---|---|---|---|---|---|
| 1 | Au/CdS/MIL-101 | HER | 25 μmol/gh | – | – | [94] |
| 2 | Au/MIL-125-$(NH_2)_2$/$TiO_2$ | OER | – | 32 μA/$cm^2$(0.75 V *vs* RHE) | 0.5 M $Na_2SO_4$ | [103] |
| 3 | Ag/MIL-125-$NH_2$/$TiO_2$ | OER | – | 1.06 mA/$cm^2$ (1.23 V *vs* RHE) | 0.5 M $Na_2SO_4$ | [90] |
| 4 | Au/ZIF-67/ZnO | OER | – | 1.93 mA/$cm^2$ (1.23 V *vs.* RHE) | 0.5 M $Na_2SO_4$ | [91] |
| 5 | α-$Fe_2O_3$@Ag@ZIF-67 | OER | – | 1.04 mA/$cm^2$ (1.23 V *vs* RHE) | 0.1 M NaOH | [57] |
| 6 | $BiVO_4$@Au@UiO-66-$NH_2$ | $CO_2$ reduction | 232.7 μmol/gh CO under 1.5 a.m. simulated sunlight | 120 μA/$cm^2$ (0.5 V *vs.* SCE) | – | [13] |
| 7 | ZIF-8/AuCu nanoprism/$TiO_2$ | $CO_2$ reduction | 86.9 μmol/gh CO under 1.5 a.m. simulated sunlight | – | – | [92] |
| 8 | $NH_2$-UiO-66/$TiO_2$/Au | $CO_2$ reduction | 26 μmol/gh $CH_4$ under 1.5 a.m. simulated sunlight | – | – | [104] |
| 9 | Ag/g-$C_3N_4$/UiO-66 | Degradation of RhB and 2,4-D | 0.01096 $min^{-1}$ for RdB and 0.00623 $min^{-1}$ for 2,4-D under visible light (λ > 420 nm) | – | – | [93] |
| 10 | ZIF-67/Ag/AgCl | MO decomposition | 0.1615 $min^{-1}$ under visible light (λ > 420 nm) | – | – | [105] |
| 11 | Ag/UiO-66/$Ag_2WO_4$ | Degradation of RhB and PBS | 0.09136 $min^{-1}$ for PBS and 0.0335 $min^{-1}$ for RhB under visible light (λ > 420 nm) | – | – | [106] |
| 12 | Ag/HKUST-1/$AgPO_4$ | PBS degradation | 0.0246 $min^{-1}$ under visible light (λ > 420 nm) | – | – | [95] |
| 13 | Au/MIL-101/$TiO_2$ | Degradation of RdB, methyl orange, methylene blue and ciprofloxacin | 2.34 ± 0.06(×$10^{-3}$ $min^{-1}$) for RdB, 3.30 ± 0.06 (×$10^{-3}$ $min^{-1}$) for methyl orange, 5.00 ± 0.01 (×$10^{-3}$ $min^{-1}$) for methylene blue and 4.62 ± 0.19(×$10^{-3}$ $min^{-1}$) for ciprofloxacin under visible light (λ > 420 nm) | – | – | [96] |
| 14 | Ag/AgCl@MIL-88A/g-$C_3N_4$ | DRN degradation | 0.0052 $min^{-1}$ under Light-Emitting Diode as light surce (power of 93.4 W, λ = 531.5 nm) | – | – | [107] |
| 15 | Ag/AgCl/MIL-100(Fe) | Degradation of RdB, tetracycline hydrochloride (TC·HCl) | 0.107 $min^{-1}$ for RdB, 0.014 $min^{-1}$ for (TC·HCl) under visible light (λ > 420 nm) | – | – | [108] |
| 16 | Ag/$Ag_3PO_4$/MIL-125-$NH_2$ | Photocatalytic reduction for Cr(VI) | 0.0621 $min^{-1}$ for Cr(VI) | | | [109] |

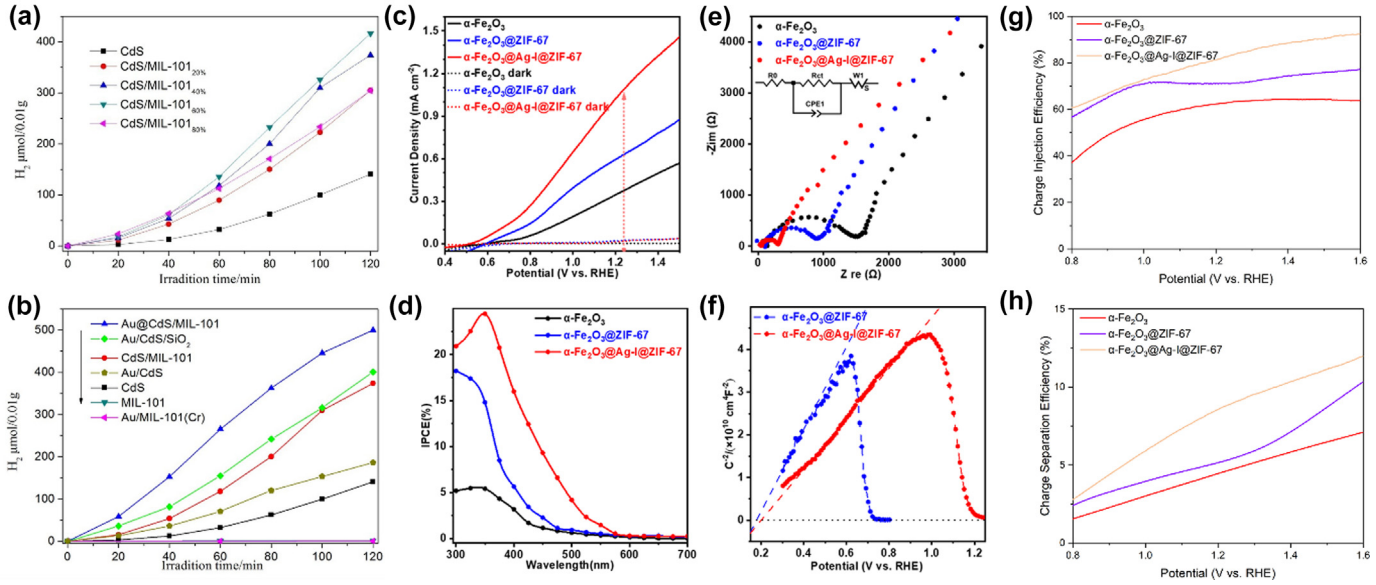


**FIG. 10**

$H_2$ evolution rates of (a) CdS with different content of MIL-101 and (b) CdS, MIL-101, Au/MIL-101, CdS/MIL-101, Au/CdS, Au/CdS/$SiO_2$ and Au@CdS/MIL-101 under visible-light illumination ($\lambda \geq 420$ nm) [94]. (c) Linear sweep voltammetry (LSV) curves of photoanodes: α-$Fe_2O_3$, α-$Fe_2O_3$@ZIF-67, α-$Fe_2O_3$@Ag-I@ZIF-67. (d) IPCE curves of measured at 1.23 V (*vs.* RHE) of the photoanodes: α-$Fe_2O_3$, α-$Fe_2O_3$@ZIF-67, α-$Fe_2O_3$@Ag-I@ZIF-67. (e) Nyquist Plot of α-$Fe_2O_3$, α-$Fe_2O_3$@ZIF-67, α-$Fe_2O_3$@Ag-I@ZIF-67 samples, with the equivalent circuit. (f) Mott-Schottky plots of α-$Fe_2O_3$@Ag-I@ZIF-67 samples. (g) Hole injection efficiency of α-$Fe_2O_3$, α-$Fe_2O_3$@ZIF-67, α-$Fe_2O_3$@Ag-I@ZIF-67 samples. (h) Bulk charge separation efficiency of α-$Fe_2O_3$, α-$Fe_2O_3$@ZIF-67, α-$Fe_2O_3$@Ag-I@ZIF-67 samples. Reproduced with permission from [57,94]. Copyright Elsevier, 2016. Copyright Elsevier, 2023.

Au/CdS/$SiO_2$, which illustrated the elevated $H_2$ evolution activity required MIL-101. Meanwhile, the $H_2$ generation rate of Au/CdS/MIL-101 was higher than CdS/MIL-101, due to improvement of electron-hole pair separation between CdS and MIL-101 when plasmonic Au nanoparticles are incorporated. Furthermore, they also demonstrated the excellent stability of Au/CdS/MIL-101 photoelectrode for water splitting [94].

Photoanodes consisting of n-type semiconductors are used for the OER process. In photoanode, the hole is the minority charge carrier, which takes part in OER. While the electron is the majority charge carrier, which migrates to the cathode via the external circuit to participate in HER due to the electron's concentration gradient [110].

Xie's group fabricated and characterised the α-$Fe_2O_3$@Ag@ZIF-67 ternary composite photoanode (Fig. 7) [57]. The highest PEC water splitting performance of α-$Fe_2O_3$@AgNR-I@ZIF-67photoelectrodes was observed (Fig. 10c). The construction of hematite@ZIF-67p-n junction improved the electron-hole pair separation (Fig. 10f, h). The ZIF-67 outlayer also elevated the surface charge transfer efficiency (Fig. 10g). The FDTD results and the better spectra overlap between Ag nanorod α-$Fe_2O_3$/ZIF-67 indicated that PRET dominated the plasmonic energy transfer from Ag to α-$Fe_2O_3$ and ZIF-67 in this system.

Zhang *et al*. studied $TiO_2$ nanorods enclosed by MIL-125-$NH_2$ and MIL-125-$(NH_2)_2$ with plasmonic Au NPs. The TEM images of the ternary nanostructured photoanode are shown in the Fig. 11a.i–ii. In this work, MIL-125-$NH_2$ and MIL-125-$(NH_2)_2$ were utilised to strengthen the photocatalytic performance of the photoanode for water splitting and the photocurrent densities of $TiO_2$/Ti-MOFs were investigated, as shown in Fig. 11a.iii. The photocurrent density of $TiO_2$/MIL-125-$(NH_2)_2$ can achieve 32 μA/$cm^2$ at 1.23 V *vs.* RHE, which is more than a 2 times enhancement of the value for bare $TiO_2$ (15μA/$cm^2$ at 1.23 V *vs.* RHE). Due to the more negative LUMO level of Ti-MOFs than the conduction band edge of $TiO_2$, there is a favourable electron transfer from Ti-MOFs to $TiO_2$, which increases the separation of charge carriers and reduces the electron-hole pair recombination. By visible light irradiation, electrons in the HOMO level of MIL-125-$NH_2$ and MIL-125-$(NH_2)_2$ are excited to the LUMO level and immediately injected into the conduction band of $TiO_2$. The excited electrons are transported through the $TiO_2$ and reach the counter electrode via the external circuit to reduce water. Simultaneously, the generated holes in the HOMO level can drive water oxidation. By loading plasmonic Au nanoparticles onto $TiO_2$/Ti-MOFs, the photocatalytic activity of the photoanode can be significantly enhanced, as shown in Fig. 11a.iv. The Au/$TiO_2$/MIL-125-$NH_2$ photoanode displayed an approximately two-fold photocurrent density increase compared to $TiO_2$ nanorods due to LSPR enhancement and light absorption extension to visible range. The photocurrent density can reach 35 uA/$cm^2$ at 1.23 V *vs.* RHE under visible light illumination. The plasmon-induced visible light absorption of Au nanoparticles enabled greater light harvesting efficiency. Meanwhile, due to the LSPR effect, a strong electromagnetic field is generated around the surface of Au nanoparticles. In addition, the photocatalytic performance of Au cannot be ignored. There is a superior enhancement of IPCE in the visible light range (420–500 nm), as shown in Fig. 11a.v, and an additional peak for Au/$TiO_2$/MIL-125-$NH_2$ at 550 nm, matching the absorption peak of Au nanoparticles. In summary, they successfully demonstrated the improved light absorption in the visible light range and improved photocatalytic performance [103].

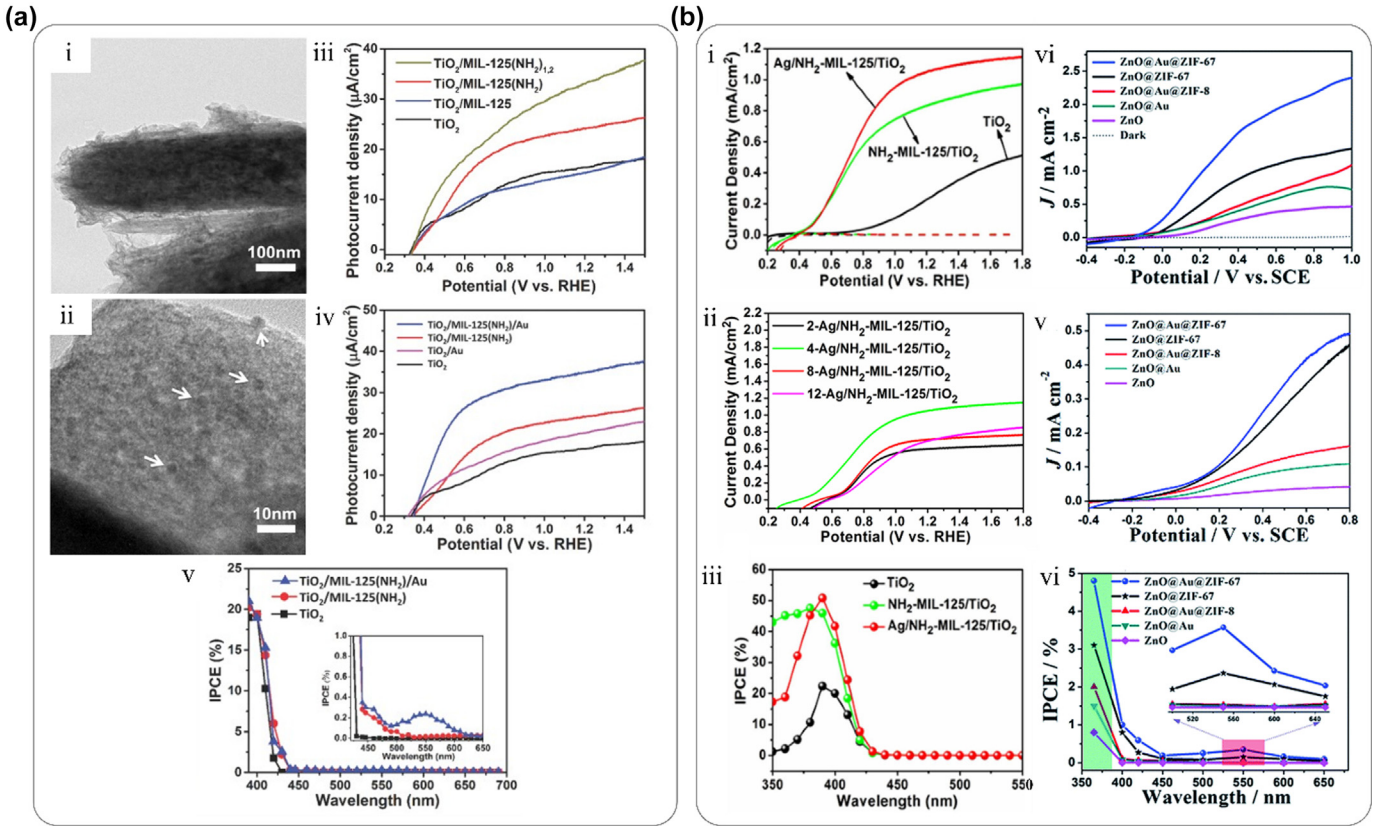


**FIG. 11**

(a) i–ii. TEM images of Au/MIL-125-$NH_2$/$TiO_2$ [103]. J-V curves of (iii) $TiO_2$/Ti-MOFs and $TiO_2$ and (iv) Au/$TiO_2$/MIL-125-$NH_2$ and other controlled photoanodes under visible light illumination (λ > 420 nm). v. IPCE results of Au/$TiO_2$/MIL-125-$NH_2$ and other controlled photoanodes under visible light irradiation (λ > 420 nm) [103]. Reproduced with permission from [103]. Copyright John Wiley and Sons, 2015. (b) i. J-V curves of Ag/MIL-125-$NH_2$/$TiO_2$ and other controlled photoanodes under 100 mW/$cm^2$ illumination and (ii) J-V curves of Ag/$NH_2$-MIL-125/$TiO_2$ with different loading content of Ag under 100 mW/$cm^2$ illumination. iii. IPCE plots of Ag/$NH_2$-MIL-125/$TiO_2$ and other controlled photoanodes [90]. iv. J-V curves of ZnO/Au/ZIF-67 and other controlled photoanodes under 100 mW/$cm^2$ illumination. v. J-V curves of ZnO/Au/ZIF-67 and other controlled photoanodes under visible light illumination (λ > 420 nm). vi. IPCE plots of ZnO/Au/ZIF-67 and other controlled photoanodes [91]. Reproduced with permission from [90,91]. Copyright Elsevier, 2020. Copyright Royal Society of Chemistry, 2017.

Compared with the limited light harvesting range of Au nanoparticles, Ag NPs possess superior capacity for light absorption between 400 and 450 nm, which is relatively matched with the heterojunction of $TiO_2$/MIL-125-$NH_2$. Cui et al. fabricated Ag NPs decorated core–shell structured $TiO_2$ nanorods-MIL-125-$NH_2$ as photoanodes for PEC water splitting. The J-V curves of Ag/MIL-125-$NH_2$/$TiO_2$ are shown in Fig. 11b.i. The PEC performance of the photoanode is enhanced by the LSPR effect and the photocurrent density can achieve 1.06 mA/$cm^2$ at 1.23 V *vs*. RHE, which is 4.42 times larger than that of pristine $TiO_2$. They also investigated the influence of Ag NP density on a PEC photoelectrode performance, shown in Fig. 11b.ii. The Ag/MIL-125-$NH_2$/$TiO_2$ also had larger IPCE value of 51% at 390 nm than $TiO_2$, which is shown in the Fig. 11b.iii. In addition, $TiO_2$/MIL-125-$NH_2$ has slightly higher IPCE value than that of Ag/MIL-125-$NH_2$/$TiO_2$ in the UV region. By loading Ag NPs, the colour of the photoanode's surface become slightly dark, which decreases the light absorption in Ultraviolet region. However, due to LSPR effect of plasmonic Ag nanoparticles, the photoanode has a larger IPCE value in the visible region [90].

Dou et al. fabricated a heterojunction photoanode consisting of Au/ZnO/ZIF-67 for PEC water splitting. As shown in Fig. 11b.iv, the Au/ZIF-67/ZnO photoanode exhibits a cathodic shift of the onset potential from 0.05 to −0.1 V and the photocurrent density of 2 mA at 0.5 V *vs*. SCE increases six-fold compared to a ZnO photoanode. Shown in Fig. 11b.vi, the IPCE value of Au/ZIF-67/ZnO and ZIF-67/ZnO photoanodes at 360 nm are 4.82% and 3.12%, a 6-fold and 4-fold increase, respectively, compared to the control photoelectrode of ZnO. Clearly, the incorporation of ZIF-67 to form a hybrid electrode clearly improved the PEC performance, as confirmed by IPCE characterisation. ZIF-67 provides more surface active sites for the catalytic reaction. Moreover, due to the extremely porous structure, it also enhances ion diffusion and $O_2$ escape. There are peaks in the region of 450–700 nm for both Au/ZIF-67/ZnO and ZIF-67/ZnO, which indicates the enhancement of visible light harvesting by ZIF-67. The photocurrent density of Au/ZIF-67/ZnO under visible light irradiation also was measured and shown in the Fig. 11b.v. In the range of visible light (greater than420 nm), the photocurrent density of Au/ZIF-67/ZnO still maintained 0.4 mA/$cm^2$ at 0.5 V

*vs.* SCE, which confirms the visible light harvesting and fast electron transfer from ZIF-67 to Au/ZnO [91].

### *Photocatalytic and photoelectrochemical $CO_2$ conversion*

The $CO_2$ cycle that produces carbohydrates for life has been carried out for thousands of years through natural photosynthesis. Recently, with the assistance of plasmonic metal/MOF/semiconductor platforms, efficient $CO_2$ conversion into carbon-based fuels has been realised. Compared with conventional semiconductors, plasmonic/MOF/semiconductor hybrid systems provide excellent $CO_2$ active sites, highly porous surfaces, and great crystallinity, which allow more $CO_2$ adsorption, a faster mass diffusion, and fewer structural defects. Therefore, $CO_2$ conversion reactions can be catalysed with a higher reactants surface concentration and shorter charge carrier diffusion length. The electron-hole pairs recombination will also be suppressed [12,111].

Dou et al. fabricated a hierarchical structured $BiVO_4$/Au/UiO-66-$NH_2$ for photocatalytic $CO_2$ reduction via growth of UiO-66-$NH_2$ on the surface of Au NPs decorated with $BiVO_4$, as shown in Fig. 12a.iii. The transfer pathway of photogenerated charges and band energy positions of $BiVO_4$/Au/UiO-66-$NH_2$ are described in the Fig. 12a.i–ii. For a $BiVO_4$/UiO-66-$NH_2$ photoelectrode, due to the p-n junction-like structure, the excited electrons in the CB of $BiVO_4$ can migrate to the CB of UiO-66-$NH_2$ without difficulty while photoinduced holes of UiO-66-$NH_2$ can transit to the VB of $BiVO_4$ as well, leading to improved charge carrier separation and fast surface $CO_2$ reduction. For Z-scheme $BiVO_4$/Au/UiO-66-$NH_2$, the excited electrons of $BiVO_4$ can transfer to the Fermi level of Au and the electrons in Au can recombine with the holes of UiO-66-$NH_2$, as shown in Fig. 12a.ii. In this case, the photogenerated holes and electrons are further separated and the kinetic process in $CO_2$ reduction is extremely enhanced. In Fig. 12a.iv, the photocurrent density under chopped-light irradiation can be observed. The $BiVO_4$/Au/UiO-66-$NH_2$ possess much higher photocurrent density than the control photoelectrodes with ~120 μA/cm$^2$ at 0.5 V *vs.* SCE. Furthermore, the photocatalytic activity for $CO_2$ reduction is evaluated, shown in Fig. 12a.v–vi. Clearly, $BiVO_4$/Au/UiO-66-$NH_2$ displays a superior product yield with 232.7 μmolh$^{-1}$g$^{-1}$ of CO and 10.18 μmolh$^{-1}$g$^{-1}$ of $CH_4$, which are higher than that of the other controlled photoelectrodes [13].

Duflot et al. synthesised the $NH_2$-UiO-66/$TiO_2$/Au composite photocatalysts [104]. The $NH_2$-UiO-66 to $TiO_2$ ratio was optimised to compromise between MOF surface area for $CO_2$ adsorption sites, visible light photons absorption capacity and a large interface contact area. The charge carrier and reaction pathways are shown in Fig. 12b.i, and the preferable metal(Zr)-to-metal(Ti) charge carrier transport pathway was ensured. Au NPs presumably act as electron traps, co-catalyst or surface plasmon resonators. Fig. 12b.ii indicates that 10 wt% $NH_2$-UiO-66/$TiO_2$/Au (at pH = 7) composite leads to the best-cumulated $CH_4$ production rate of 136 μmol/$g_{catalyst}$ with 70% electronic selectivity over 5 h of the continuous test.

Butburee and co-workers developed a ternary photocatalyst system with plasmonic AuCu nanoprisms embedded between a porous single crystalline $TiO_2$ nanoplate thin film and ZIF-8 nanoparticles for photocatalytic $CO_2$ reduction. The photocatalytic performance for $CO_2$ reduction of AuCu/ZIF-8/$TiO_2$ (sample 3J-2DT) has superior total production yield (CO + $CH_4$) of 86.9 μmolh$^{-1}$g$^{-1}$, which is nearly a 21-fold increase compared to that of bare $TiO_2$, as shown in Fig. 12b.iv. In Fig. 12b.v, the time-course evolution of CO and $CH_4$ from $CO_2$ on 3J-2DT and 2J-2DT is illustrated. Due to the nearly linear curves of products yield with time, excellent photocatalytic stabilities of 3J-2DT and 2J-2DT are both confirmed. The novel design enabled high density photoinduced charges from the AuCu-$TiO_2$ interface with high density $CO_2$ absorption on ZIF-8 to achieve remarkable $CO_2$ convention efficiency [92].

### *Other photocatalytic and PEC environmental applications*

In addition to the applications in water splitting and $CO_2$ reduction, ternary photoelectrodes consisting of plasmonic/MOF/semiconductor could also be applied for other environmental applications.

General environmental applications includes (i) NOx, $NH_3$ and VOC decomposition in air, (ii) Selective chemical contaminant decomposition in water, (iii) Pollutant and degradation product detection, (iv) Plasmonic-conjugated polymer catalysts for pollutant decomposition. Yet, most of the plasmonic/MOF/semiconductor composites reported have be focused on the degradation of organic pollutants.

By chemical protonation coating and photodeposition, Feng et al. fabricated a complex ternary photoelectrode Ag/g-$C_3N_4$/UiO-66 for degradation of rhodamine B (RhB) dye and 2,4-dichlorophenoxyacetic acid (2,4-d) [93]. By incorporation of plasmonic Ag NPs and g-$C_3N_4$, separation and mobility of photoinduced charges as well as visible light absorption are all effectively enhanced. The microstructure and morphology of the photoelectrode is shown in Fig. 8a–b. In their work, the band structure diagram of the photoelectrode is established to explain the mechanism of its superior photocatalytic performance, as shown in Fig. 8c. The CB value of g-$C_3N_4$ is more negative than the CB value of UiO-66, the electron transportation from the CB of g-$C_3N_4$ to the CB of UiO-66 can occur. Thus, the recombination of photoinduced charges can be mitigated. Moreover, decorated Ag NPs can not only serve as electron transfer bridges to evolute separation of charge carriers, but also excite more electrons in the visible light region by the SPR effect. Since the electron potential in the CB of g-$C_3N_4$ is lower than $O_2$/$^{\cdot}O_2^-$, the generated electrons can react with $O_2$ to produce $^{\cdot}O_2^-$. In addition, due to the lower VB value of g-$C_3N_4$ than the standard $E_0$ ($^{\cdot}OH/H_2O$), photoinduced holes cannot oxidize $H_2O$ to produce $^{\cdot}OH$. However, the holes can destroy RhB and 2,4-d directly, so both generated $^{\cdot}O_2^-$ and holes can degrade RhB and 2,4-d. Meanwhile, the excited electrons of UiO-66 react with $H_2O_2$ to form $^{\cdot}OH$ as well as $Zr^{4+}$ to produce $Zr^{3+}$ in the Zr-O clusters in UiO-66. The $Zr^{3+}$ can reduce $O_2$ absorbed to form $^{\cdot}O_2^-$. Furthermore, UiO-66 provide more catalytic active sites in liquid phase, which potentially accelerate the reaction. An Ag/g-$C_3N_4$/UiO-66 photoelectrode exhibits superior photocatalytic performance for degradation of RhB and 2,4-d. The highest reaction rate constant of Ag/g-$C_3N_4$/UiO-66 for RhB and 2,4-d degradation are 0.01096 min$^{-1}$ and 0.00623 min$^{-1}$, which are 26.7 and 18.8 times of that than g-$C_3N_4$ respectively [93].

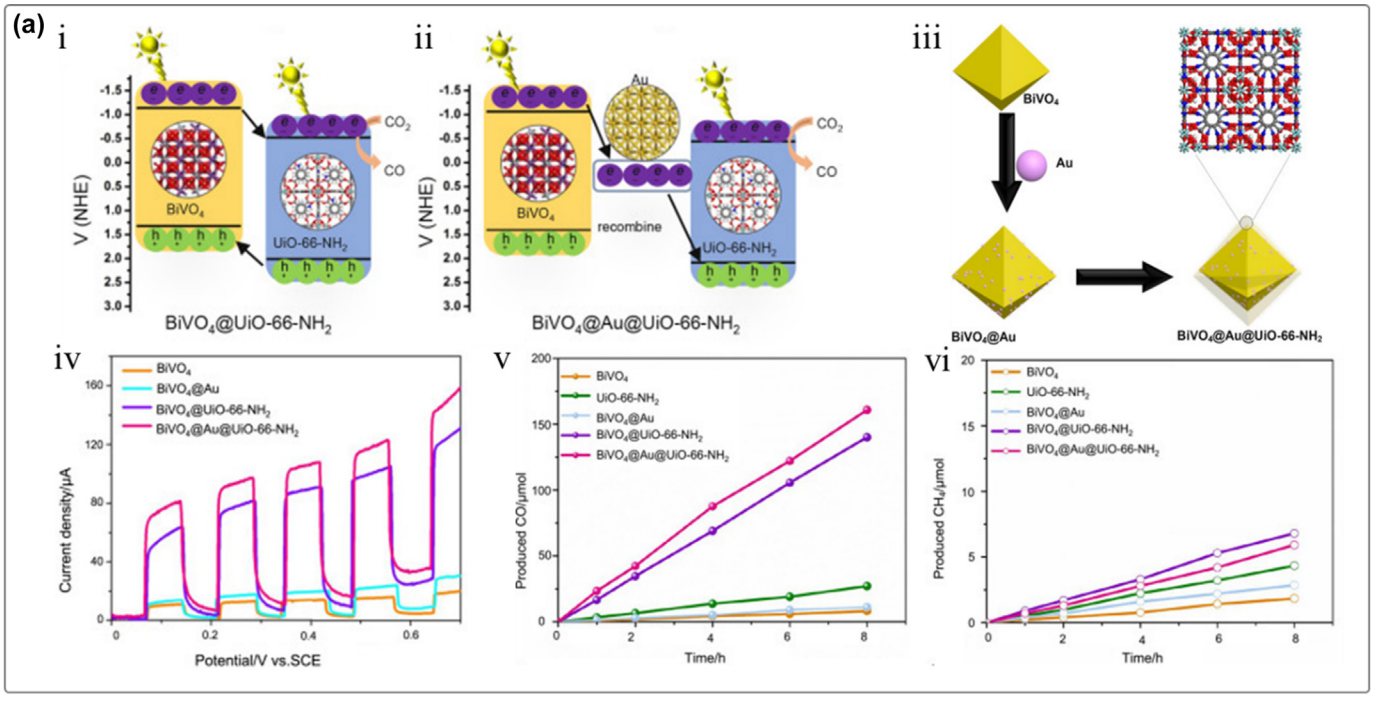


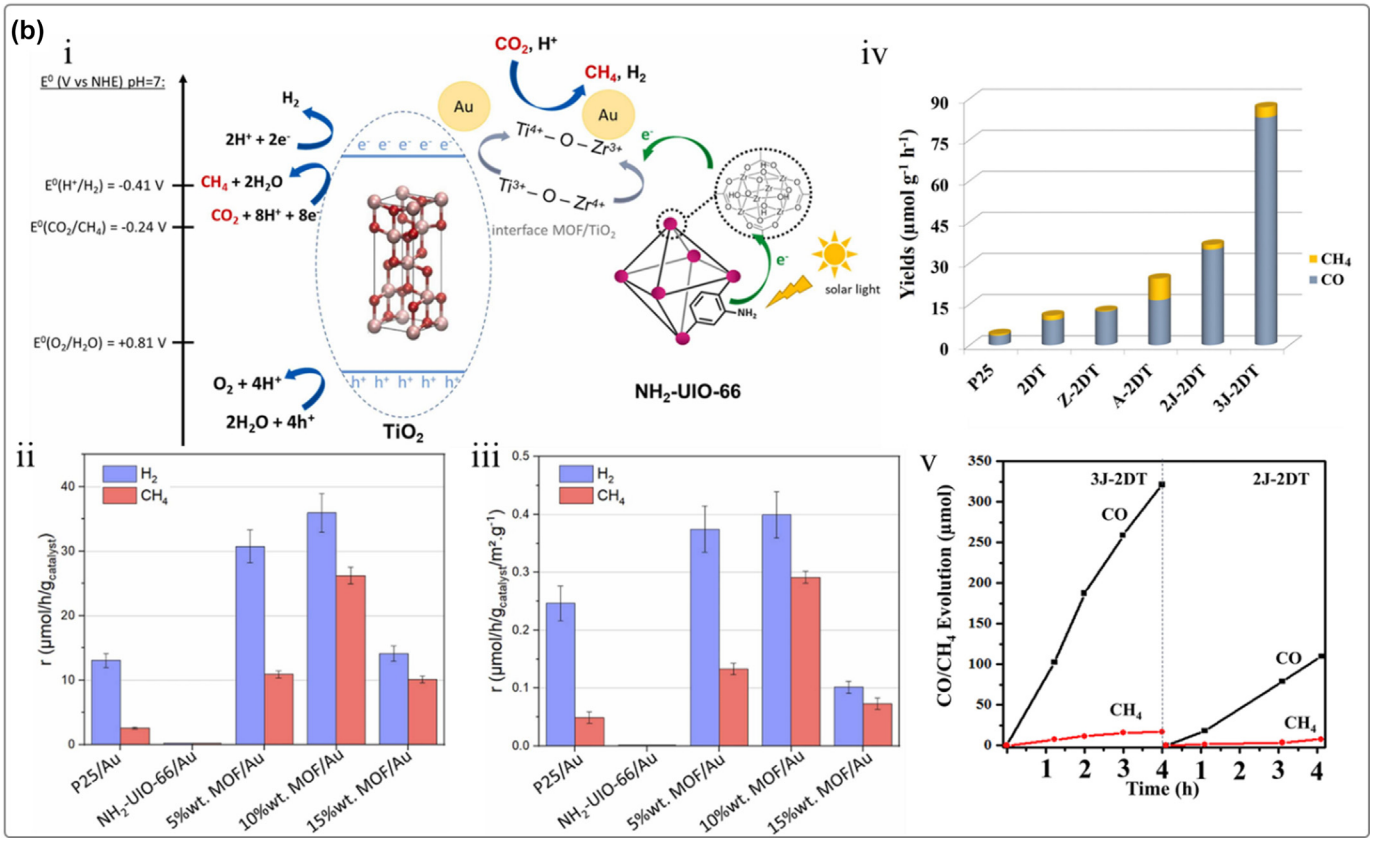


**FIG. 12**

(a) i. Fabrication process of $BiVO_4$/Au/UiO-66-$NH_2$. Schematic illustration of the electron and hole separation routes in (ii) $BiVO_4$/UiO-66-$NH_2$ and (iii) $BiVO_4$/Au/UiO-66-$NH_2$ [13]. vi. J-V curves, v. CO yield, vi. $CH_4$ yeild of $BiVO_4$/Au/UiO-66-$NH_2$ and other controlled photoelectrodes under chopped-light illumination [13]. Reproduced with permission from [13]. Copyright Elsevier, 2020. (b) i. Schematic charge carrier and reaction pathways on $NH_2$-UiO-66/$TiO_2$ composites. ii. Specific $H_2$ (blue) and $CH_4$ (red) average production rate in presence of water vapor (during 5 h) under continuous CO2 flow (0.3 mL/min) and under solar light irradiation on $NH_2$-UiO-66/$TiO_2$ composites at pH = 7 (at 5, 10 and 15 wt% MOF), and average production rate in function of $S_{BET}$ on (iii) $NH_2$-UiO-66/$TiO_2$ composites at pH = 7 (at 5, 10 and 15 wt% MOF). (iv) Production yields of CO and $CH_4$ in $CO_2$ photocatalytic reduction on AuCu/ZIF-8/$TiO_2$ and various controlled samples. (v) Time-course productions of CO and $CH_4$ in $CO_2$ photocatalytic reduction on 3J-2DT and 2J-2DT [92]. Reproduced with permission from [92]. Copyright Elsevier, 2019. Reproduced with permission from [104]. Copyright Elsevier, 2023.

In 2020, Shao and co-workers developed a novel ternary photocatalyst of ZIF-67/AgCl/Ag for Methyl Orange (MO) decomposition by chemical etching, deposition–precipitation and a light-induced reduction approach [105]. The band structure diagram of the photocatalyst is established and exhibited in Fig. 13a. As can be seen, SPR-excited electrons of Ag can be transferred to the CB of AgCl through the Ag-AgCl interfaces, which can facilitate MO degradation. Meanwhile, ZIF-67 can easily absorb visible light due to its lower band gap energy (1.92 eV). The photoinduced electrons can recombine with holes in the VB of Ag simultaneously. Furthermore, ·OH can be formed from OH— oxidation by excited holes. Therefore, ·OH and excited electrons can both decompose MO. Instead of monodirectional transportation of excited electrons in Ag nanoparticles, the photoinduced electrons also can be transferred to both MOF and semiconductor in the heterojunction of Ag/UiO-66/$Ag_2WO_4$.

Sofi et al. reported a novel design of Ag/UiO-66/$Ag_2WO_4$ as photocatalyst under visible light for photodegradation of RhB and Ponceau BS (PBS). The schematic band structure diagram of Ag/UiO-66/$Ag_2WO_4$ is shown in the Fig. 13b. Due to the wide band gap of UiO-66 and $Ag_2WO_4$, visible light cannot be absorbed directly. By the SPR effect of plasmonic Ag NPs, generated electron- hole pairs can be separated under visible light irradiation and excited electrons can be transferred to UiO-66 and $Ag_2WO_4$. The generated electrons in the CB of UiO-66 can reduce $O_2$ to form $\cdot O_2$—. Due to more positive potential of CB of $Ag_2WO_4$ than the standard redox potential of $O_2/\cdot O_2$—, $O_2$ reduction cannot occur. Furthermore, ·OH can not only be produced by reaction of the $H_2O_2$ that is formed from $O_2$ and the excited electrons in the CB of $Ag_2WO_4$ but also generated through water oxidation by holes on the surface of Ag. The equations are exhibited in Fig. 13a as well. The photocatalytic activity of Ag/UiO-66/$Ag_2WO_4$ is demonstrated in the Fig. 13d–e. Compared with other controlled photocatalysts, Ag/UiO-66/$Ag_2WO_4$ exhibits the highest photocatalytic efficiency (0.09136 $min^{-1}$ for PBS and 0.0335 $min^{-1}$ for RhB), which is due to the enhanced charge carrier separation, deduction of recombination and extension of light absorption under visible light [106]. In 2018, Sofi and co-workers also designed a ternary photocatalysts of Ag/HKUST-1/$AgPO_4$ for PBS degradation. The photocatalytic performance of PBS degradation under visible light irradiation was also shown. Clearly, Ag/HKUST-1/$AgPO_4$ possesses the highest photocatalytic efficiency (0.0246 $min^{-1}$), which is 6 times higher than pristine HKUST-1 with enhanced charge separation, a decrease of the recombination and an SPR effect of Ag NPs [95].

Wang's research group has presented an additional instance involving ternary composites comprising Ag/$Ag_3PO_4$/MIL-125-$NH_2$ for the purpose of photocatalytic reduction of Cr(VI) [109]. Upon exposure to illumination, $Ag_3PO_4$ and MIL-125-$NH_2$ engender the generation of electron-hole pairs. In this context, photo-induced electrons traverse from $Ag_3PO_4$ to Ag(0), while holes migrate from MIL-125-$NH_2$ to Ag(0), driven by the alignment of band energy levels. Notably, Ag(0) functions as an electron transfer mediator, thereby enhancing the efficacy of charge separation. This mechanism results in the suppression of charge recombination on MIL-125-$NH_2$, leading to a heightened influx of electrons available for facilitating the reduction of Cr(VI).

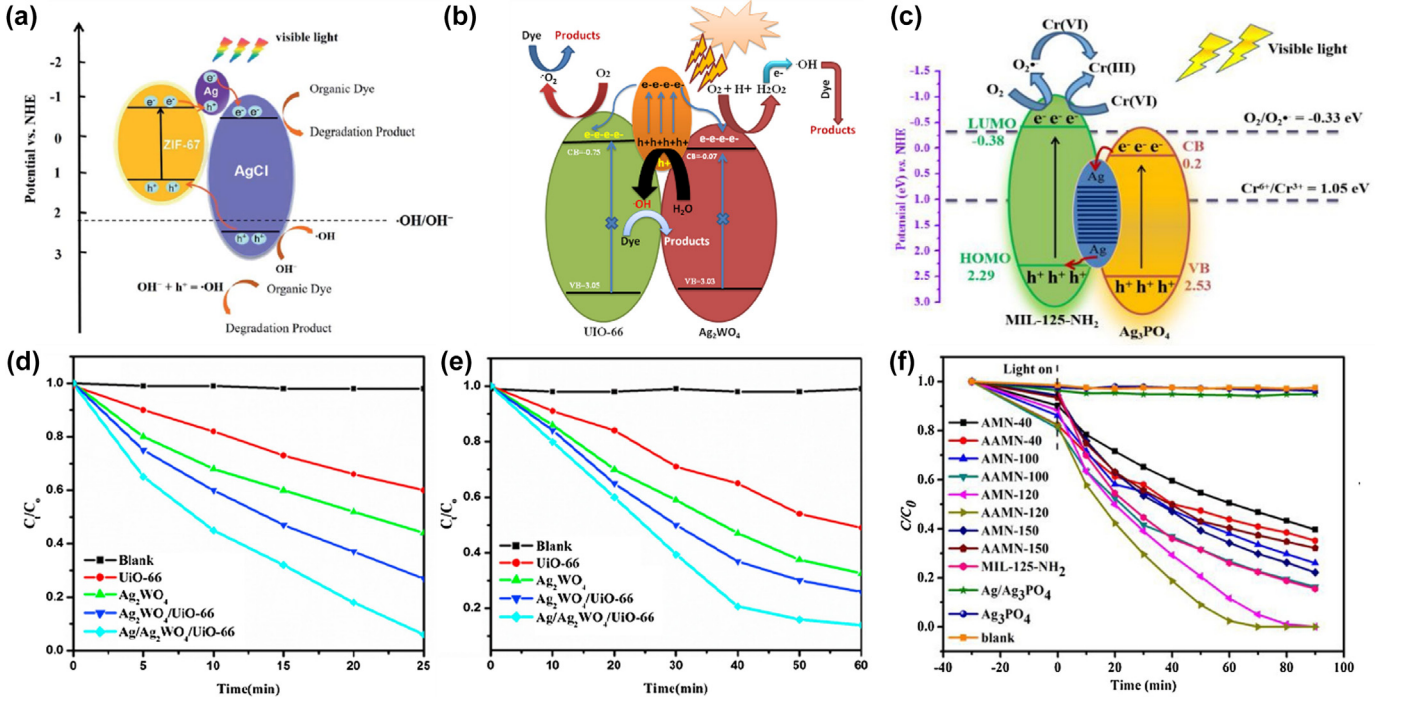


**FIG. 13**

(a) Band structure diagram of Ag/AgCl/ZIF-67 [105]. (b) Schematic diagram showing the band of Ag/$Ag_2WO_4$/UiO-66 under visible light irradiation [106]. (c) Band alignment diagram of Ag/$Ag_3PO_4$/MIL-125-$NH_2$ and mechanism of photocatalytic Cr(VI) cleanup [109]. The degradation efficiency of (d) PBS and (e) RhB in the presence of Ag/$Ag_2WO_4$/UiO-66. (f) The photocatalytic performance of samples prepared toward Cr(VI). Reproduced with permission from [105,106,109]. Copyright Royal Society of Chemistry, 2020. Copyright Elsevier, 2019. Copyright Elsevier, 2020.

The optimised $Ag/Ag_3PO_4/MIL\text{-}125\text{-}NH_2$ composite exhibits a reaction rate of 0.0621 $min^{-1}$. This impressive rate surpasses that of $MIL\text{-}125\text{-}NH_2$ by a factor of 2.77, and remarkably, it is 124.2 times greater than that of $Ag_3PO_4$.

Akgün, and Dükkanc synthesised a series of g-$C_3N_4$ supported Ag/AgCl doped MIL-88A composite materials (Fig. 14a–e) to evaluate their photodegradation performance for a herbicide diuron (DRN) used in agriculture [107]. The optimised Ag/AgCl@MIL-88A/g-$C_3N_4$ (ACM-gC-7, Fe:Ag mole ratio 0.25:0.75) material show considerably higher photoactivity to that of a single component (MIL-88A) and double component (MIL-88A/g-$C_3N_4$) in the visible-light and degrade nearly 100% DRN on irradiation for 1 h without using any oxidant (Fig. 14f). At the same time, ACM-gC-7 completely degrade DRN in 15 min and 30 min on the use of $H_2O_2$ or persulfate (PS) (Fig. 14g), respectively. Thus, this work highlights that the construction of a ternary system attributed to the effective charge carriers separation through Z-scheme formation, whereas the surface plasmon resonance (SPR) effect of Ag nanoparticles, significantly accelerates the charge transfer and the absorption efficiency of the light absorber involved in photocatalytic reaction. Through the schematic energy diagram reported in Fig. 14h-i, Akgün, and Dükkanc also proposed the DRN degradation mechanism over MIL-88A/g-$C_3N_4$ and Ag/AgCl@MIL-88A/g-$C_3N_4$, respectively.

Quite similar work had been reported earlier by Chen et al., where they constructed a Z-scheme hybrid materials by control coating of MIL-100(Fe) MOF on plasmonic Ag/AgCl nanowire for boosting visible light photodegradation of organic pollutants (rhodamine B (Rh B) and tetracycline hydrochloride (TC·HCl)) (Fig. 15) [108]. The schematic illustration reported in Fig. 15a provides the morphology associated with the synthesis procedure and the corresponding SEM, TEM, HR-TEM and TEM-EDX elemental mapping images (Fig. 15b–i) substantiate the construction of Ag/AgCl/MOFs core–shell nanowire (ACN). The improved photocatalytic performance of MIL-100(Fe) on conjugating with plasmonic Ag/AgCL nanorods has been confirmed by evaluating the light absorbance efficiency and photodegradation of organic pollutants (Fig. 15j–l).

Additionally, plasmonic Au nanoparticles also are utilised. Tilgner and Kempe developed a core–shell structured Au/MIL-101/anatase as a photocatalyst under visible light illumination for the degradation of RdB, methyl orange, methylene blue and ciprofloxacin. The Au/MIL-101/anatase possesses a rate constant of 2.34 ± 0.06 ($\times 10^{-3} min^{-1}$) and a convention rate of 59% under the selected conditions and the excellent stability during 5 times cycle can be confirmed as well. By measurement and calculation, the rate constants for the degradation of methyl orange, methylene and ciprofloxacin can achieve 3.30 ± 0.06 ($\times 10^{-3} min^{-1}$), 5.00 ± 0.01 ($\times 10^{-3} min^{-1}$) and 4.62 ± 0.19 ($\times 10^{-3} min^{-1}$) respectively [96].

## Summary and future perspectives

For decades, researchers have extensively explored methods to improve the performance of semiconductor-based photoelectrodes via doping, morphology control *etc*. Considering the three basic steps of PC/PEC catalysis: the absorption of photons, the separation of electron-hole pairs, and charge transportation for reacting with water molecules. Plasmonic nanostructures could build SPP and LSPR fields, which promote light absorption and charge separation. While MOFs could expand the spectral light absorption range. The porous structure of MOFs favours the charge and mass transport for the surface redox reaction. Therefore, we review emerging plasmon-MOF-based materials for photoelectrodes and propose the ternary Plasmon-MOF-semiconductor structure, which takes advantage of both MOFs and plasmons and is listed in Table 2. This could potentially be an effective strategy for reliable photoelectrodes for large-scale light harvesting technology. However, these approaches are still at their infant stage for commercial applications. The efficiency

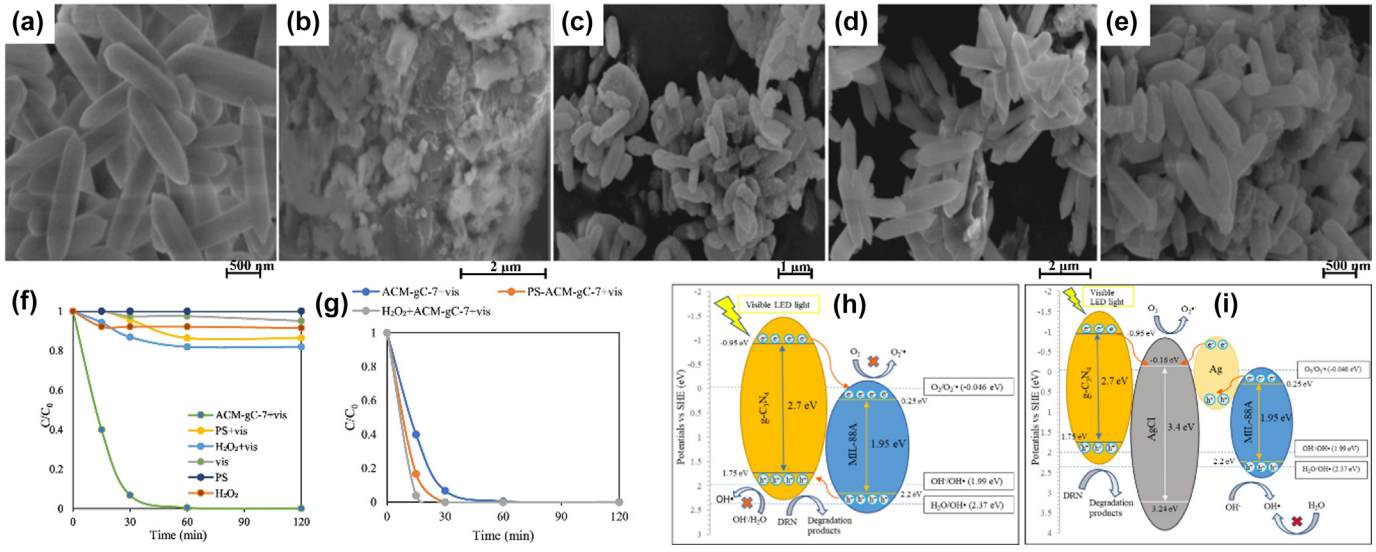


**FIG. 14**

SEM micrographs of (a) MIL-88A, (b) g-$C_3N_4$, (c) Ag/AgCl@MIL-88A, (d) MIL-88A/g-$C_3N_4$, and (e) Ag/AgCl@MIL-88A/g-$C_3N_4$ (ACM-gC-7) samples. Photodegradation of DRN in various degradation processes (f), and (g) aqueous matrix over ACM-gC-7 composite. Charge transfer mechanism over (h) MIL-88A/g-$C_3N_4$ and (i) Ag/AgCl@MIL-88A/g-$C_3N_4$ under visible LED light irradiation. Reproduced with permission from [107]. Copyright Elsevier, 2023.

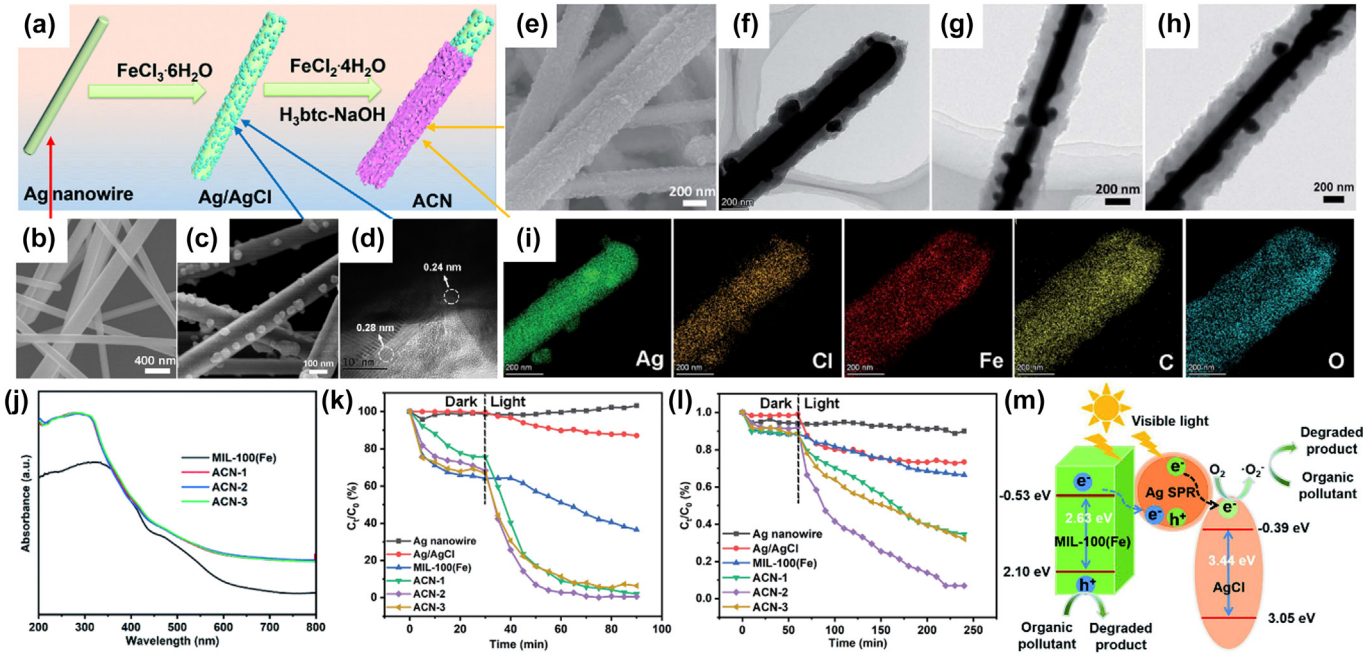


**FIG. 15**

(a) Schematic presentation of the morphology of the products and the synthesis process of Ag/AgCl/MOFs core–shell nanowire (ACN). SEM images of (b) Ag nanowire, (c) Ag/AgCl nanowire and (d) HR-TEM image of Ag/AgCl nanowire. (e) SEM image of ACN-2 sample. TEM images of (f) ACN-1, (g) ACN-2, and (h) ACN-3 samples. (i) TEM-EDX mapping images of Ag, Cl, Fe, C, and O elements in ACN-1 sample. (j) UV–visible diffuse reflection spectra of pure MIL-100 (Fe), ACN-1, ACN-2 and ACN-3 samples. Photocatalytic degradation of (k) rhodamine B (Rh B), and (l) tetracycline hydrochloride (TC·HCl). (m) Schematic of photodegradation of organic pollutants over the ACN series under light irradiation. Reproduced with permission from [108]. Copyright Royal Society of Chemistry, 2022.

of the photoelectrodes hardly achieves the requirement of practical use. The cycling stability of the ternary photoelectrodes is rarely studied and reported, especially in high-temperature environments and strong bases. Due to the limitation of the large number of synthesized MOFs, the ternary heterojunctions with MOFs are hard to be utilised in commercial products. During the decades of research, there still is a huge quantity of other MOFs with redox-active metals and/or functional organic linkers to be explored. Non-noble plasmonic metal is also in potential. We believe that new ternary photoelectrodes with higher efficiency and excellent cycling stability in water splitting, $CO_2$ reduction and photodegradation of organic pollutants will be explored and developed in the near future. The development of new ternary photoelectrodes holds immense potential for transforming sustainable technologies related to energy conversion, net zero, circular economy, and environmental remediation. Despite the challenges involved, the synergy between different materials and their ability to be designed and tailored to the specific applications offers exciting opportunities for advancing the field of photoelectrochemistry and sustainability. Ternary photoelectrodes, which combine three different materials with complementary properties, have the potential to achieve higher energy conversion efficiencies compared to binary or single-component materials. Through careful selection and optimization of these materials, researchers can create synergistic effects that enhance light absorption, charge separation, and catalytic activity, leading to improved conversion of solar energy into chemical fuels. This could result in significant economic and environmental benefits, driving the adoption of these technologies on a larger scale. Furthermore, plasmonic metal-incorporated ternary photoelectrodes can be designed to perform multiple tasks simultaneously, as the tailored interactions between different components (photocatalyst, plasmonic metal, and MOFs) enable efficient utilization of solar energy for various applications.

## CRediT authorship contribution statement

**Chengyu Ji:** Conceptualization, Investigation, Writing – original draft. **Haochen Zhou:** Investigation. **Sixing Tang:** Investigation. **Pankaj Sharma:** Investigation, Writing – review & editing. **Mary P. Ryan:** Investigation. **D. Jason Riley:** Supervision, Writing – review & editing. **Fang Xie:** Conceptualization, Supervision, Writing – review & editing.

## Data availability

No data was used for the research described in the article.

## Declaration of Competing Interest

The authors declare that they have no known competing financial interests or personal relationships that could have appeared to influence the work reported in this paper.

## Acknowledgements

F.X. acknowledges the Henry Royce Institute made through EPSRC grant EP/R00661X/1, EPSRC programme grant EP/W017075/1 and the Royal Society International Exchange grant IEC/NSFC/191390.

## References


[1] C.A. Ogunbode, R. Doran, G. Böhm, Clim. Change 158 (2020) 361–375.
[2] C. by fuel type-Exajoules, C.D. Emissions, bp Statistical Review of World Energy June 2020, (2020).
[3] Hydrogen Production Technical Team Roadmap, (n.d.) 98. https://www.energy.gov/eere/fuelcells/articles/hydrogen-production-technical-team-roadmap.
[4] E.L. Miller, R. Garland, II.G.1 Photoelectrochemical Hydrogen Production: DOE PEC Working Group Overview, (2010) 7.
[5] T. Hisatomi, J. Kubota, K. Domen, Chem. Soc. Rev. 43 (2014) 7520–7535, https://doi.org/10.1039/c3cs60378d.
[6] R. Saravanan, F. Gracia, A. Stephen, Basic principles, mechanism, and challenges of photocatalysis, in: Nanocomposites for Visible Light-Induced Photocatalysis, Springer, 2017, pp. 19–40, https://doi.org/10.1007/978-3-319-62446-4.
[7] J. Zhang et al., Mechanism of photocatalysis, in: Photocatalysis, Springer, 2018, pp. 1–15. https://www.springerprofessional.de/en/mechanism-of-photocatalysis/16948932.
[8] D. Zhou, K. Fan, Chin. J. Catal. 42 (2021) 904–919, https://doi.org/10.1016/S1872-2067(20)63712-3.
[9] X.T. Xu et al., Adv. Sci. 6 (2019) 1801505, https://doi.org/10.1002/advs.201801505.
[10] S. Horike, S. Kitagawa, Design of porous coordination polymers/metal–organic frameworks: past, present and future, in: Metal-Organic Frameworks, John Wiley & Sons Ltd, 2011, pp. 1–21, https://doi.org/10.1002/9783527635856.ch1.
[11] Q. Yang, Q. Xu, H.L. Jiang, Chem. Soc. Rev. 46 (2017) 4774–4808, https://doi.org/10.1039/C6CS00724D.
[12] C.S.L. Koh et al., ACS Mater. Lett. 3 (2021) 557–573, https://doi.org/10.1021/acsmaterialslett.1c00047.
[13] Y. Dou et al., Chem. Eng. 1 (2020) 48–55, https://doi.org/10.1016/j.gce.2020.09.009.
[14] Y. Wang et al., Angew. Chem. Int. Ed. 59 (2020) 4365–4369, https://doi.org/10.1002/anie.201915807.
[15] Y.Z. Li et al., Inorg. Chem. Front. 7 (2020) 746–755, https://doi.org/10.1039/C9QI01262A.
[16] S. Gaikwad et al., J. Environ. Chem. Eng. 9 (2021), https://doi.org/10.1016/j.jece.2021.105523 105523.
[17] W.J. Ji et al., CrstEngComm 22 (2020) 4710–4715, https://doi.org/10.1039/D0CE00457J.
[18] X. Huang et al., ACS Appl. Mater. Interfaces 13 (2021) 3471–3480, https://doi.org/10.1021/acsami.0c20799.
[19] X. Liu et al., ACS Appl. Mater. Interfaces 13 (2021) 9643–9655, https://doi.org/10.1021/acsami.0c21486.
[20] M. Oggianu et al., Magnetochemistry. 6 (2020) 39, https://doi.org/10.3390/magnetochemistry6030039.
[21] A. Gu et al., Appl. Surf. Sci. 516 (2020), https://doi.org/10.1016/j.apsusc.2020.146160 146160.
[22] J. Li, N. Wu, Sci. Technol. 5 (2015) 1360–1384, https://doi.org/10.1039/C4CY00974F.
[23] L. Sun, M.G. Campbell, M. Dincă, Angew. Chem. Int. Ed. 55 (2016) 3566–3579, https://doi.org/10.1002/anie.201506219.
[24] H. Li et al., Nature 402 (1999) 276–279, https://doi.org/10.1038/46248.
[25] M. Alvaro et al., Eur. J. 13 (2007) 5106–5112, https://doi.org/10.1002/chem.200601003.
[26] B. Pattengale et al., Exceptionally Long-Lived Charge Separated State in Zeolitic Imidazolate Framework: Implication for Photocatalytic Applications, (2016). https://doi.org/10.1021/jacs.6b04615.
[27] J. Zhang et al., Chem. Eng. J. 385 (2020), https://doi.org/10.1016/j.cej.2019.123814 123814.
[28] A. Melillo et al., Appl. Catal. B 278 (2020), https://doi.org/10.1016/j.apcatb.2020.119345 119345.
[29] G. Zhong, D. Liu, J. Zhang, J. Mater. Chem. A 6 (2018) 1887–1899, https://doi.org/10.1039/C7TA08268A.
[30] J. Zheng, Z. Jiao, J. Colloid Interface Sci. 488 (2017) 234–239, https://doi.org/10.1016/j.jcis.2016.11.007.
[31] X.-Y. Dao et al., Inorg. Chem. 58 (2019) 8517–8524, https://doi.org/10.1021/acs.inorgchem.9b00824.
[32] C.F. Cogswell, Z. Xie, S. Choi, Tuning of metal-organic frameworks by pre- and post-synthetic functionalization for catalysis and separations, in: Metal-Organic Frameworks, John Wiley & Sons Ltd, 2018, pp. 297–339, https://doi.org/10.1002/9783527809097.ch10.
[33] S. Mandal et al., Adv. Funct. Mater. 31 (2021) 2006291, https://doi.org/10.1002/adfm.202006291.
[34] Z. Yin et al., Coord. Chem. Rev. 378 (2019) 500–512, https://doi.org/10.1016/j.ccr.2017.11.015.
[35] K.T. Butler, C.H. Hendon, A. Walsh, Faraday Discuss. 201 (2017) 207–219, https://doi.org/10.1039/C7FD00019G.
[36] X. Wang et al., ACS Appl. Mater. Interfaces 8 (2016) 9080–9087, https://doi.org/10.1021/acsami.6b00028.
[37] J.W. Yoon et al., Appl. Catal. B 244 (2019) 511–518, https://doi.org/10.1016/j.apcatb.2018.11.057.
[38] Y. Xiao et al., J. Energy Chem. 58 (2021) 508–522, https://doi.org/10.1016/j.jechem.2020.10.008.
[39] K. Zhang et al., Small Sci. 1 (2021) 2100060, https://doi.org/10.1002/smsc.202100060.
[40] L. Lu et al., Inorg. Chem. Front. 6 (2019) 3456–3467, https://doi.org/10.1039/C9QI00964G.
[41] J. Low et al., Adv. Mater. 29 (2017) 1601694, https://doi.org/10.1002/adma.201601694.
[42] A. Kuila et al., Appl. Surf. Sci. 553 (2021), https://doi.org/10.1016/j.apsusc.2021.149556 149556.
[43] S. Subudhi et al., J. Colloid Interface Sci. 568 (2020) 89–105, https://doi.org/10.1016/j.jcis.2020.02.043.
[44] J. Low, J. Yu, C. Jiang, Design and fabrication of direct Z-scheme photocatalysts, in: Interface Science and Technology, Elsevier, 2020, pp. 193–229, https://doi.org/10.1016/B978-0-08-102890-2.00006-3.
[45] H. Yang et al., Nano Res. 12 (2019) 643–650, https://doi.org/10.1007/s12274-019-2272-4.
[46] N. Askari et al., Chemosphere 251 (2020), https://doi.org/10.1016/j.chemosphere.2020.126453 126453.
[47] S.K. Bhardwaj et al., J. Mater. Chem. A 6 (2018) 14992–15009, https://doi.org/10.1039/C8TA04220A.
[48] W. Cui et al., Electrochim. Acta 349 (2020), https://doi.org/10.1016/j.electacta.2020.136383 136383.
[49] J.E. Mondloch et al., Chem. Commun. 50 (2014) 8944–8946, https://doi.org/10.1039/C4CC02401J.
[50] J.-W. Yoon et al., Adv. Energy Mater. n/a (n.d.) 2003052. https://doi.org/10.1002/aenm.202003052.
[51] W. Zhu et al., Appl. Catal. B 238 (2018) 339–345, https://doi.org/10.1016/j.apcatb.2018.07.024.
[52] X. Deng et al., Small 15 (2019) 1902287, https://doi.org/10.1002/smll.201902287.
[53] M. Chen et al., Nanotechnology 29 (2018), https://doi.org/10.1088/1361-6528/aabdb1 284003.
[54] D. Jin et al., Microchim. Acta 182 (2015) 1885–1892, https://doi.org/10.1007/s00604-015-1505-9.
[55] H.-Q. Xu et al., ACS Catal. 8 (2018) 11615–11621, https://doi.org/10.1021/acscatal.8b03233.
[56] J.-D. Xiao, H.-L. Jiang, Acc. Chem. Res. 52 (2019) 356–366, https://doi.org/10.1021/acs.accounts.8b00521.
[57] C. Ji et al., Mater. Today Adv. 18 (2023), https://doi.org/10.1016/j.mtadv.2023.100361 100361.
[58] L. Mascaretti et al., Adv. Mater. (2019) 1805513, https://doi.org/10.1002/adma.201805513.
[59] S. Zeng et al., Chem. Soc. Rev. 43 (2014) 3426–3452, https://doi.org/10.1039/C3CS60479A.
[60] Y. Wu et al., Chinese Phys. B 27 (2018), https://doi.org/10.1088/1674-1056/27/12/126101 126101.
[61] W.L. Barnes, J. Opt. A Pure Appl. Opt. 8 (2006) S87–S93, https://doi.org/10.1088/1464-4258/8/4/S06.
[62] N. Wu, Nanoscale 10 (2018) 2679–2696, https://doi.org/10.1039/C7NR08487K.
[63] Q. Jiang et al., Nanomaterials 9 (2019) 1, https://doi.org/10.3390/nano9010001.
[64] P. Zhang, T. Wang, J. Gong, Adv. Mater. 27 (2015) 5328–5342, https://doi.org/10.1002/adma.201500888.
[65] Y. Zhang et al., Chem. Rev. 118 (2018) 2927–2954, https://doi.org/10.1021/acs.chemrev.7b00430.
[66] A.O. Govorov, H. Zhang, Y.H. Gun'ko, J. Phys. Chem. C 117 (2013) 16616–16631, https://doi.org/10.1021/jp405430m.
[67] A. Furube et al., J. Am. Chem. Soc. 129 (2007) 14852–14853, https://doi.org/10.1021/ja076134v.
[68] Y. Lv, S. Duan, R. Wang, Progr. Natural Sci.: Mater. Int. 30 (2020) 1–12, https://doi.org/10.1016/j.pnsc.2019.12.005.

[69] R. Jiang et al., Adv. Mater. 26 (2014) 5274–5309, https://doi.org/10.1002/adma.201400203.
[70] C.-C. Wang et al., Chemosphere 303 (2022), https://doi.org/10.1016/j.chemosphere.2022.134949 134949.
[71] X. Li et al., Chem. Commun. 54 (2018) 1917–1920, https://doi.org/10.1039/C7CC09072B.
[72] G. Jia et al., Appl. Surf. Sci. 448 (2018) 254–260, https://doi.org/10.1016/j.apsusc.2018.04.102.
[73] C. Zhang, L. Ai, J. Jiang, J. Mater. Chem. A 3 (2015) 3074–3081, https://doi.org/10.1039/C4TA04622F.
[74] Q. Zhang et al., Sol. Energy 171 (2018) 388–396, https://doi.org/10.1016/j.solener.2018.06.086.
[75] X. Du et al., Chin. J. Catal. 40 (2019) 70–79, https://doi.org/10.1016/S1872-2067(18)63160-2.
[76] H. Yasmeen et al., J. Chin. Chem. Soc. 67 (2020) 1611–1617, https://doi.org/10.1002/jccs.202000205.
[77] D.V. Dao et al., Appl Catal. B 286 (2021), https://doi.org/10.1016/j.apcatb.2021.119947 119947.
[78] H. Jung, Y. Whang, S.W. Han, Bull. Kor. Chem. Soc. 42 (2021) 806–809, https://doi.org/10.1002/bkcs.12270.
[79] R. Fu et al., Mater. Chem. Phys. 267 (2021), https://doi.org/10.1016/j.matchemphys.2021.124702 124702.
[80] C. Mao et al., ACS Nano 11 (2017) 9010–9021, https://doi.org/10.1021/acsnano.7b03513.
[81] O. Akhavan, J. Colloid Interface Sci. 336 (2009) 117–124, https://doi.org/10.1016/j.jcis.2009.03.018.
[82] J. Li et al., Nat. Commun. 4 (2013) 2651, https://doi.org/10.1038/ncomms3651.
[83] O. Guselnikova et al., Anal. Chim. Acta 1068 (2019) 70–79, https://doi.org/10.1016/j.aca.2019.03.058.
[84] J. Briscoe, Zirconium metal-organic framework functionalized plasmonic sensor, in: J.A. Guicheteau, C.R. Howle (Eds.), Chemical, Biological, Radiological, Nuclear, and Explosives (CBRNE) Sensing, XX, SPIE, Baltimore, United States, 2019, p. 14, https://doi.org/10.1117/12.2519134.
[85] X. Zhao et al., Chin. J. Catal. 42 (2021) 872–903, https://doi.org/10.1016/S1872-2067(20)63715-9.
[86] G. Zheng et al., Plasmonic metal-organic frameworks, SmartMat n/a (n.d.). https://doi.org/10.1002/smm2.1047.
[87] J.-D. Xiao et al., Angew. Chem. 128 (2016) 9535–9539, https://doi.org/10.1002/ange.201603990.
[88] K.M. Choi et al., J. Am. Chem. Soc. 139 (2017) 356–362, https://doi.org/10.1021/jacs.6b11027.
[89] H. Robatjazi et al., Sci. Adv. 5 (2019) eaav5340, https://doi.org/10.1126/sciadv.aav5340.
[90] W. Cui et al., Chem. Eng. J. 388 (2020), https://doi.org/10.1016/j.cej.2020.124206 124206.
[91] Y. Dou et al., J. Mater. Chem. A 5 (2017) 19491–19498, https://doi.org/10.1039/C7TA06443H.
[92] T. Butburee et al., Nano Energy 62 (2019) 426–433, https://doi.org/10.1016/j.nanoen.2019.05.060.
[93] S. Feng et al., Res. Chem. Intermed. 45 (2019) 1263–1279, https://doi.org/10.1007/s11164-018-3682-8.
[94] Y. Wang et al., Appl. Catal. B 185 (2016) 307–314, https://doi.org/10.1016/j.apcatb.2015.12.020.
[95] F.A. Sofi, K. Majid, O. Mehraj, J. Alloys Compd. 737 (2018) 798–808, https://doi.org/10.1016/j.jallcom.2017.12.141.
[96] D. Tilgner, R. Kempe, Chem. – Eur. J. 23 (2017) 3184–3190, https://doi.org/10.1002/chem.201605473.
[97] Y. Gutiérrez et al., J. Appl. Phys. 128 (2020), https://doi.org/10.1063/5.0020752 080901.
[98] Z. Li et al., Anal. Chem. 90 (2018) 961–967, https://doi.org/10.1021/acs.analchem.7b04015.
[99] M. Wang, Y. Tang, Y. Jin, ACS Catal. 9 (2019) 11502–11514, https://doi.org/10.1021/acscatal.9b03971.
[100] W. Wang et al., Adv. Sci. 4 (2017) 1600371, https://doi.org/10.1002/advs.201600371.
[101] J.-D. Xiao et al., Angew. Chem. Int. Ed. 57 (2018) 1103–1107, https://doi.org/10.1002/anie.201711725.
[102] J. Guo et al., Nano Res. (2020), https://doi.org/10.1007/s12274-020-3182-1.
[103] L. Zhang et al., Adv. Sci. 3 (2016) 1500243, https://doi.org/10.1002/advs.201500243.
[104] M. Duflot et al., Catal. Today 413–415 (2023), https://doi.org/10.1016/j.cattod.2023.01.025 114018.
[105] W. Shao et al., RSC Adv. 10 (2020) 38174–38183, https://doi.org/10.1039/D0RA06842J.
[106] F.A. Sofi, K. Majid, Chem. Phys. Lett. 720 (2019) 7–14, https://doi.org/10.1016/j.cplett.2019.02.005.
[107] D. Akgün, M. Dükkanc , J. Water Process Eng. 51 (2023), https://doi.org/10.1016/j.jwpe.2022.103469 103469.
[108] X. Chen et al., RSC Adv. 12 (2022) 3119–3127, https://doi.org/10.1039/D1RA08576J.
[109] Y.-C. Zhou et al., Chin. Chem. Lett. 31 (2020) 2645–2650, https://doi.org/10.1016/j.cclet.2020.02.048.
[110] P. Dias, A. Mendes, Hydrogen production from photoelectrochemical water splitting, in: R.A. Meyers (Ed.), Encyclopedia of Sustainability Science and Technology, Springer, New York, NY, 2017, pp. 1–52, https://doi.org/10.1007/978-1-4939-2493-6_957-1.
[111] X. Li, Q.-L. Zhu, EnergyChem 2 (2020), https://doi.org/10.1016/j.enchem.2020.100033 100033.